Multiple constraints on regional CO2 flux variations over land and oceans

Philippe Peylin, Philippe Bousquet, C. Le Quéré, S. Sitch, P. Friedlingstein,
G. Mckinley, N. Gruber, P. Rayner, Philippe Ciais

Multiple constraints on regional CO$_2$ flux variations over land and oceans

Philippe Peylin,[1] Philippe Bousquet,[2,3] Corinne Le Quéré,[4] Stephen Sitch,[5,6]
Pierre Friedlingstein,[2] Galen McKinley,[7] Nicolas Gruber,[8] Peter Rayner,[9]
and Philippe Ciais[2]

[1] To increase our understanding of the carbon cycle, we compare regional estimates of CO$_2$ flux variability for 1980–1998 from atmospheric CO$_2$ inversions and from process-based models of the land (SLAVE and LPJ) and ocean (OPA and MIT). Over the land, the phase and amplitude of the different estimates agree well, especially at continental scale. Flux variations are predominantly controlled by El Niño events, with the exception of the post-Pinatubo period of the early 1990s. Differences between the two land models result mainly from the response of heterotrophic respiration to precipitation and temperature. The "Lloyd and Taylor" formulation of LPJ [*Lloyd and Taylor*, 1994] agrees better with the inverse estimates. Over the ocean, inversion and model results agree only in the equatorial Pacific and partly in the austral ocean. In the austral ocean, an increased CO$_2$ sink is present in the inversion and OPA model, and results from increased stratification of the ocean. In the northern oceans, the inversions estimate large flux variations in line with time-series observations of the subtropical Atlantic, but not supported by the two model estimates, thus suggesting that the CO$_2$ variability from high-latitude oceans needs further investigation.

Citation: Peylin, P., P. Bousquet, C. Le Quéré, S. Sitch, P. Friedlingstein, G. McKinley, N. Gruber, P. Rayner, and P. Ciais (2005), Multiple constraints on regional CO$_2$ flux variations over land and oceans, *Global Biogeochem. Cycles*, *19*, GB1011, doi:10.1029/2003GB002214.

1. Introduction

[2] Year-to-year fluctuations in the atmospheric CO$_2$ growth rate (Figure 2a in section 3.1) are one of the clearest signals of the global carbon cycle. Those fluctuations are of the same magnitude as the long-term annual mean accumulation in the atmosphere. They are caused mostly by the impact of climate variability on the ocean and land carbon reservoirs, since fossil fuel emissions increase smoothly year to year. The existence of interannual variability (IAV) in the carbon cycle shows that CO$_2$ fluxes react to varying climate patterns in a fairly coherent manner at large spatial scales, despite strong heterogeneity at small spatial scales. Understanding of the IAV signal is necessary to assess the future response of the carbon cycle to climate change [*Cox et al.*, 2000].

[3] The IAV has been the object of numerous studies, aiming at deciphering which of the ocean or land exchange causes the largest fluctuation. Those studies belong either to the so-called "top-down" atmospheric approach or to the "bottom-up" approach (predictions from biogeochemical models or in situ observations).

[4] Top-down studies used atmospheric observations of CO$_2$ [*Keeling et al.*, 1995], CO$_2$ and δ^{13}C [*Keeling et al.*, 1996; *Francey et al.*, 1995; *Joos et al.*, 1999], and O$_2$:N$_2$, ^{13}C, and CO$_2$ [*Battle et al.*, 2000] to apportion the global IAV signal between land and oceans, with conflicting results. Some of the differences, particularly those involving δ^{13}C, can be attributed to differences in δ^{13}C data sets linked to the difficulty in maintaining an accurate ^{13}C calibration. Other studies [*Ciais et al.*, 1995; *Rayner et al.*, 1999; *Keeling and Piper*, 2001] similarly used CO$_2$ and δ^{13}C to estimate the IAV in carbon fluxes over broad latitude bands. In recent years, modelers have estimated IAV in

---

[1]Laboratoire Biogéochimie des Milieux Continentaux INRA-CNRS-UPMC, INRA-INAPG, Thiverval-Grignon, France.
[2]Laboratoire des Sciences du Climat et de l'Environnement, Commissariat à l'Energie Atomique, Gif sur Yvette, France.
[3]Also at Université de Versailles Saint Quentin en Yvelines, Versailles, France.
[4]Max-Planck-Institut für Biogeochemie, Jena, Germany.
[5]Potsdam Institut für Klimafolgenforschung (PIK), Potsdam, Germany.
[6]Now at MetOffice (JCHMR), Wallingford, UK.
[7]Department of Atmospheric and Oceanic Sciences, University of Wisconsin-Madison, Madison, Wisconsin, USA.
[8]IGPP and Department of Atmospheric Sciences, University of California, Los Angeles, California, USA.
[9]CSIRO Atmospheric Research, Aspendale, Victoria, Australia.

regional carbon fluxes using synthesis inversions based on three-dimensional (3-D) atmospheric transport models and on time series of gradients in atmospheric CO$_2$ at nearly 100 stations around the globe [*Bousquet et al.*, 2000; *Rödenbeck et al.*, 2003]. *Bousquet et al.* [2000] suggested through a series of sensitivity tests that the terrestrial biosphere was the main contributor of IAV in fluxes, both globally and regionally. *Rödenbeck et al.* [2003] estimated flux IAV at the resolution of their transport model (8° × 10°) using only CO$_2$ data, and reached similar conclusions, but highlight a correlation between IAV of terrestrial fluxes and biomass burning activity as inferred from remotely sensed fire counts [*Schimel and Baker*, 2002]. The idea that biomass burning could be a major player in the IAV of fluxes also emerged from a multiple species analysis by *Langenfelds et al.* [2002].

[5] "Bottom-up" studies used process-based biogeochemical models in climate models [*Jones et al.*, 2001] or forced by climate fields to quantify regional IAV of carbon fluxes over land [*Kindermann et al.*, 1996; *Tian et al.*, 1998; *Knorr*, 2000; *Gerard et al.*, 1999; *Botta et al.*, 2002] and over the ocean [*Le Quéré et al.*, 2003b; *McKinley et al.*, 2004; *Winguth et al.*, 1994]. Although those studies all agree in suggesting that the land IAV is larger than the ocean IAV, they may not attribute the IAV phenomenon to the same processes, and different models exhibit large discrepancies in the IAV regional signal [*McGuire et al.*, 2001]. Furthermore, some potentially important processes such as ecosystem disturbance (including fire fluxes) [*Zimov et al.*, 1999; *van der Werf et al.*, 2003] or the enhancement of air-sea gas exchange by storms [*Bates*, 2002] are often missed in carbon models. Bottom-up modeling of the IAV is also difficult to validate against direct observations of the fluxes because of the scarcity of long time series of carbon flux measurements over land [*Baldocchi et al.*, 2001; *Goulden et al.*, 1996] as well as over the ocean [*Gruber et al.*, 2002; *Lee et al.*, 2002a].

[6] In addition to IAV in the climate fields used to drive carbon cycle models, a significant IAV signal also shows up in time series of satellite indexes of the vegetation greenness [*Myneni et al.*, 1997; *Braswell et al.*, 1997], despite specific problems of long-term satellite data sets. There is still a knowledge gap to interpret interannual fluctuations in the vegetation greenness in terms of net carbon fluxes by the means of models [*Lucht et al.*, 2002].

[7] Among the most salient questions raised by the IAV of carbon fluxes is its link with the El Niño–Southern Oscillation (ENSO) and other modes of climate variability. El Niño has long been observed to be synchronous with higher than normal CO$_2$ growth rates [*Keeling et al.*, 1989; *Gaudry*, 1993; *Bacastow*, 1976]. Also, the observation of lower than normal growth rate directly after the climate cooling induced by the Pinatubo eruption in 1991 and the follow-up return to normal growth rates in 1994 remains largely unexplained, and may be related to the effect of cooler temperatures on respiration, or with a temporary increase in the diffuse fraction of downwelling solar radi-

ation increasing canopy photosynthesis [*Farquhar and Roderick*, 2003; *Gu et al.*, 2003]. In both cases, the underlying processes are poorly understood.

[8] The scale at which top-down and bottom-up methods estimate the IAV is different. The two approaches do not fully support or exclude each other, unless the atmospheric data can be downscaled significantly. In this paper, we compare CO$_2$ surface flux IAV inferred from atmospheric inversions together with independent calculations from two terrestrial carbon models and two ocean carbon models. The inversion work is an extended analysis of work by *Bousquet et al.* [2000] that includes assessment of errors. The comparison is performed at global and regional levels. Here we consider "regional" to represent continents or large ocean basins. We discuss reasons for agreement and disagreement, and the limitations of the comparison, and we analyze the processes that control the IAV in the bottom-up models.

2. Methodology

2.1. Atmospheric Inversions: Top-Down Fluxes

[9] We use a Bayesian synthesis inverse model [*Enting*, 2002] to retrieve the net CO$_2$ fluxes every month from 1980 to 1998. The method has been explained by *Bousquet et al.* [2000] and is based on the work of *Peylin et al.* [1999]. Details can be found in these papers or in Appendix A. We solve for the monthly land and ocean fluxes (11 and 8 regions, respectively, Figure 1) in order to minimize both the distance between model responses and observations and the distance between a priori fluxes and optimized fluxes, using specific weights (errors). Sixty-eight stations are used (see location and year of first assimilation in Figure 1). Errors on the data are calculated monthly at each site either from the standard deviation of the residuals from raw flask measurements and a smooth curve (if more than four individual/pairs of flasks are sampled during a month) when available, otherwise from the mean standard deviation provided by National Oceanic and Atmospheric Administration (NOAA) [2000]. A minimum error value of 0.5 ppm is applied to account for other sources of uncertainties such as instrumental errors, possible calibration offsets between networks, etc. Land fluxes are assigned prior monthly values (balanced annually and with no IAV) and prior geographic patterns within each region from the SIB-2 global biosphere model [*Denning et al.*, 1996]. Ocean fluxes are assigned prior values and patterns (no IAV) from a global synthesis of air-sea-flux measurements [*Takahashi et al.*, 1997]. Prior errors on net fluxes are set to $\pm 1/\sqrt{12}$ GtC month^{-1} (1 GtC annually), identically over land and ocean regions. Such loosely defined errors help to regularize the solution but do not nudge the solution of the inversion to the prior estimates. Model responses are calculated with the TM2 transport model [*Heimann*, 1995].

[10] As all causes of uncertainties cannot be explicitly accounted for in such inversion, we carried out a series (seven) of inversions as in work by *Bousquet et al.* [2000] (see Appendix A) to investigate the sensitivity of our results. We varied the transport model (TM3 instead of TM2), the meteorological fields (1993 instead of 1990), the
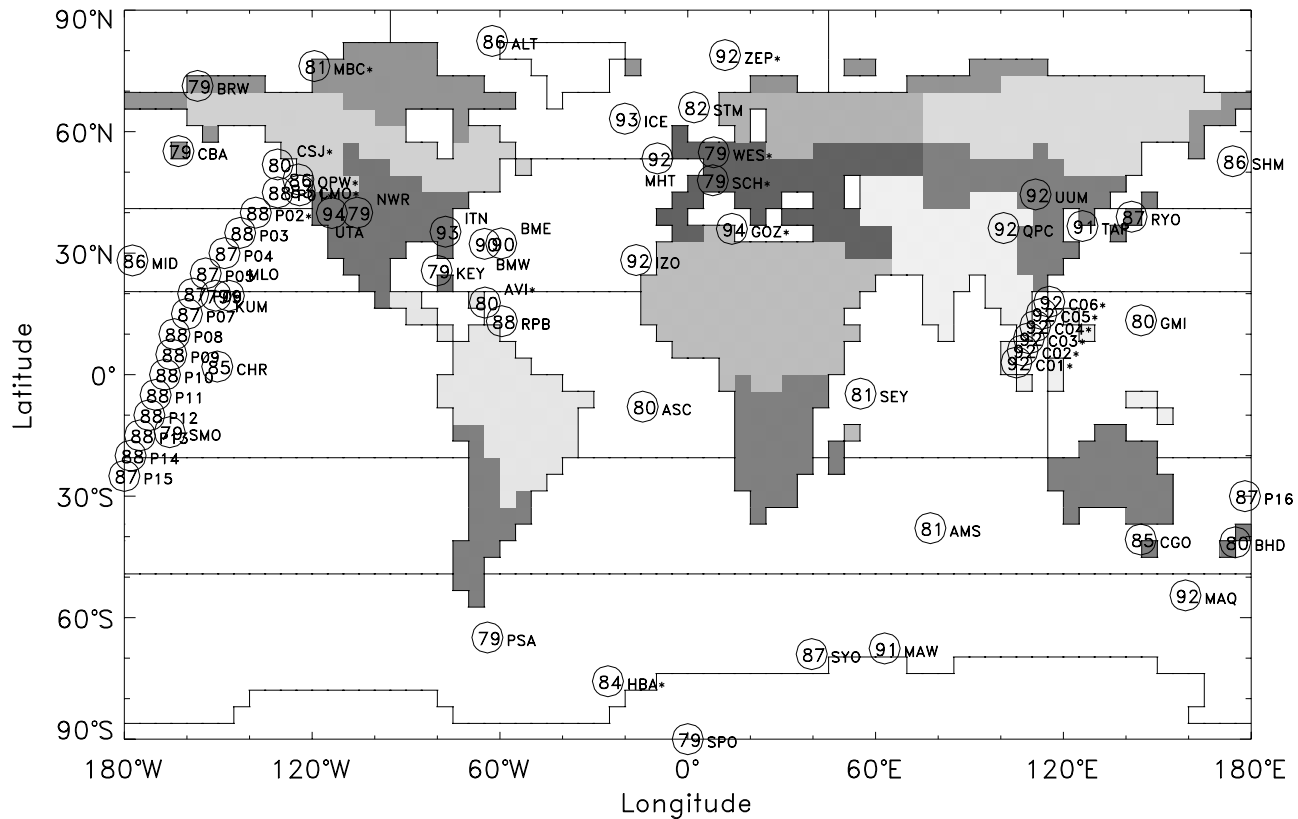
Figure 1. Map of the different regions used in the inversions for the standard case: 11 land regions and 11 oceanic regions. The location and acronyms of the stations used in this study are also shown together with the year when the monitoring started. Asterisks denote sites that ended before the end of the inversion (ZEP* 96; MBC* 96; WES* 98; CSJ* 91; OPW* 89; SCH* 98; CMO* 96; P01* 94; P02* 95; GOZ* 97; C06* 97; AVI* 89; C05* 97; C04* 97; C03* 97; C02* 97; C01* 97; HBA* 97).

number of regions (30 instead of 19), the errors on observations (multiplied by 2), the number of observations (20 stations covering 1980–1998 instead of an increasing number with time), the constraint on global oceanic sink (removed), and the type of observations (using deseasonalized CO$_2$ data).

[11] As seen in Figure 1, most of the stations appeared gradually between the early 1980s to mid-1990s (especially in the Northern Hemisphere). Our choice of increasing the number of stations in the network (as opposed to *Rödenbeck et al.* [2003]) follows the objective of utilizing all available data, given the underdetermined nature of our inverse problem. However, it is a potential source of bias, and one should always try to verify that any given flux anomaly does not directly corresponds to the addition or removal of any particular sites (see section 4.1).

[12] As a further sensitivity experiment, we include an independent inversion estimate of fluxes over the same period, labeled "Rayner-inv" on the figures. This monthly inversion using 26 land/ocean regions is an update of *Rayner et al.* [1999]. The differences from that work can be summarized as follows: (1) The δ^{13}C record has been revised using a new calibration scheme, (2) the input CO$_2$, δ^{13}C, and O$_2$/N$_2$ records have been extended forward in time up to 1998, (3) the atmospheric response functions

have been recalculated with a different transport model, MATCH/MACCM2 [*Gurney et al.*, 2002], and (4) a term has been added to the δ^{13}C budget to treat the dilution of δ^{13}C anomalies by the gross fluxes (see Appendix A). "Rayner-inv" is different from the above ensemble of inversions in almost every significant respect (transport model, data, the use of δ^{13}C), and therefore the two studies provide a reasonable consistency check on the top-down estimates.

2.2. Land Biosphere Models: LPJ and SLAVE

[13] We use two process-based biosphere models in this study: the Lund-Potsdam-Jena Dynamic Global Vegetation Model (LPJ-DGVM) [*Sitch et al.*, 2003; *Smith et al.*, 2001], which combines vegetation dynamics and biogeochemistry, and the SLAVE terrestrial biogeochemistry model [*Friedlingstein et al.*, 1995]. Both models simulate land-atmosphere carbon exchange, driven by seasonal and interannual variations in climate. However, formulation (and number) of processes primarily responsible for this exchange differ among models. The major characteristics and differences with respect to carbon exchange are summarized in Table 1 with further details given in Appendix B1. Overall, SLAVE can be considered a less complex biospheric model than LPJ. However, in terms of

Table 1. Major Characteristics of the Two Land-Atmosphere Carbon Exchange Models, LPJ and SLAVE

	LPJ	SLAVE
PFTs[a]	10	10
NPP	GPP and autotrophic respiration	light use efficiency
f()	APAR, gs, Ci, Ca, T, Cleaf,...	APAR, LAI, SRAD, T,...
	Farquhar et al. [1980]	*Field et al.* [1995]
Nitrogen	no	no
Heterotrophic Respiration	first-order kinetics	first-order kinetics
Pools	4	3
Temperature control	"Arrhenius" [*Lloyd and Taylor*, 1994]	"Q10"
Water control	yes	yes [*Parton et al.*, 1993]
Land use	no	no
Natural biomass burning	yes	no
Nutrients feedbacks	no	on CO$_2$ fertilization only
		Friedlingstein et al. [1995]
Light diffuse versus direct	no	no

[a]Plant functional types.

interannual carbon fluxes, the models will mainly differ because of their heterotrophic respiration formulation.

2.3. Ocean Carbon Models: OPA and MIT

[14] Air-sea CO$_2$ fluxes are modeled with two offline biogeochemical models, coupled, respectively, to the MIT and OPA ocean general circulation model [*McKinley et al.*, 2003; *Le Quéré et al.*, 2003a]. Model carbon fluxes differ not only by the physical fields but also by the biogeochemical processes, as summarized in Table 2 and detailed in Appendix B2.

3. Results

[15] We discuss the monthly varying flux anomalies (after removing the long-term seasonal cycle) and extend some previous analysis of *Bousquet et al.* [2000] using the bottom-up estimates.

3.1. Global Fluxes

[16] Over the 1980–1998 period, the annual accumulation of CO$_2$ in the atmosphere has shown variations of ±1.5 ppm (Figure 2a), reflecting surface flux anomalies. The inverse estimates for global land and ocean fluxes are compared with predictions of SLAVE and LPJ land models and OPA and MIT OCE models and with the inverse results of [*Rayner et al.*, 1999] (updated version). The gray zone represents the envelope of our ensemble (seven) of inversions.

[17] One should first mention that the spread between all the inversions for the flux IAV is relatively small compared

to the spread obtained for the mean annual fluxes (not shown). Indeed, the mean global land uptake for the 1980–1998 period varies within a factor of 3 between the seven inversions (0.7 to 2.0 GtC yr^{-1}). This corroborates the result discussed initially by *Bousquet et al.* [2000] and further by *Rödenbeck et al.* [2003], that we have more confidence in the IAV of surface fluxes retrieved by the inversions than on net fluxes. IAV indeed relies on temporal changes of the concentration differences between stations, which can be larger than the mean concentration differences (e.g., between Atlantic and Pacific stations the difference varies between ±0.5 ppm compared to a mean difference close to 0.2 ppm over the 1990s; see *Bousquet et al.* [2000, Figure 4]). A common feature between the "top-down" and "bottom-up" approaches is that they all produce more flux IAV (peak to peak amplitude) over land (around ±2 GtC yr^{-1}) than over oceans (around ±0.7 GtC yr^{-1}). For the bottom-up approaches, this is quite remarkable as the land and ocean biogeochemical models do not have explicit links. For the top-down approaches, note that we use equal prior weights but that the land plus ocean anomalies (minus fossil) must match globally the anomalous growth rate.

[18] The phase of modeled and inverted land fluxes is closely correlated with growth rate anomalies ($r = 0.87$ with our mean inversion), especially during El Niño events (1982–1983, 1987–1988, and 1997–1998) when land ecosystems tend to accumulate less or even release carbon (Figure 2b). At this global scale, the two inverse approaches are highly correlated ($r = 0.73$) but the peak to peak amplitude of the "Rayner-inv" estimate is slightly smaller

Table 2. Major Characteristics of the Two Ocean-Atmosphere Carbon Exchange Models, OPA and MIT

|	MIT	OPA
Grid size	latitude 0.3°–1°; longitude 1°	latitude 0.5°–1.5°; longitude 2°
Forcing data	NCEP/COADS	NCEP/ECMWF/ERS
Restoring of *T* and *S*	none	below the mixed layer poleward of 15°
Restoring of tracers	below 1000 m	none
Biogeochemistry	particle export	NPZD
Alkalinity	function of salinity	function of salinity
Air-sea gas exchange	*Wanninkhof* [1992]	*Wanninkhof* [1992]
Mean air-sea flux, GtC/yr	1.8	1.5
Flux STD, GtC/yr	0.28	0.24
Dominant IAV region	equatorial Pacific	equatorial Pacific
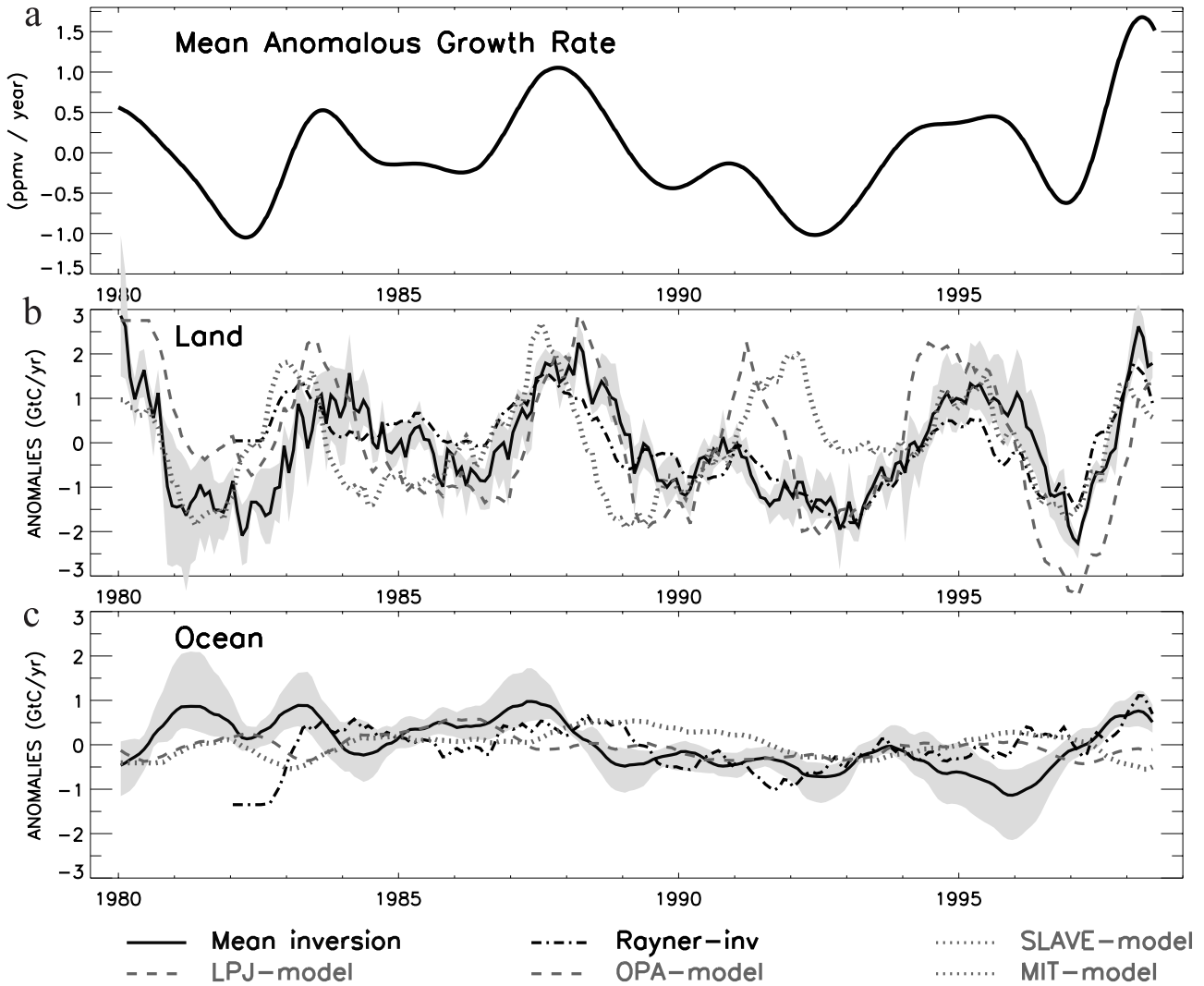
Figure 2. (a) Mean anomalous gross rate obtained from the data at all stations of Figure 1. (b, c) Global land and global ocean flux anomalies over 1980–1998 (in GtC per year) as obtained from our ensemble of inversions (gray zone defines the range of all inversions, and dark line denotes the mean), from *Rayner et al.* [1999], from the SLAVE land surface model [*Friedlingstein et al.*, 1995], from the LPJ land surface model [*Sitch et al.*, 2003], from the OPA-HAMOCC3 ocean model [*Le Quéré et al.*, 2000], and from the MIT ocean model [*McKinley et al.*, 2003]. See color version of this figure at back of this issue.

than that of our mean inversion. Given the large differences between the two inversion setups, such an agreement gives us some confidence in the inverse results at this scale. There is also a strikingly good agreement between the inversions and the land models. The amplitude of the signals are rather similar, with standard deviations of 1.1 and 1.5 and 1.0 GtC yr^{-1}, for SLAVE, LPJ, and our mean inversion, respectively. As for the phase, LPJ roughly follows the inversions, whereas SLAVE model presents on average a 6-month negative lag (larger for the 1982–1983 and 1987–1988 El Niño events). The correlation coefficients (*r*) after correction of the lags are 0.7 and 0.5, respectively (those values remain quite small because large intra-annual fluctuations, still present in the inverse estimates, decrease the value of *r*). The main difference between top-down and bottom-up approaches is found in the early 1990s after the

Pinatubo eruption when very low growth rates occurred. We will come back to this period in section 4.1. One should also notice the strong agreement between all approaches for 1997–1998 major El Niño (especially in the phase of the IAVs), a period with a much larger number of atmospheric stations compared to the 1980s.

[19] For ocean fluxes (Figure 2c), all flux estimates present smaller IAVs than their land counterpart with standard deviations on the order of 0.5 GtC yr^{-1} for the two inversions and 0.25 GtC yr^{-1} for the bottom-up approaches (OPA and MIT). The largest peak to peak amplitude of the anomalies is found in our set of inversions. These different estimates also do not agree in phase for most of the 20-year period with a correlation coefficient lower than 0.3. Differences between "Rayner-inv" inversion, our inversions and the two bottom-up approaches are of the
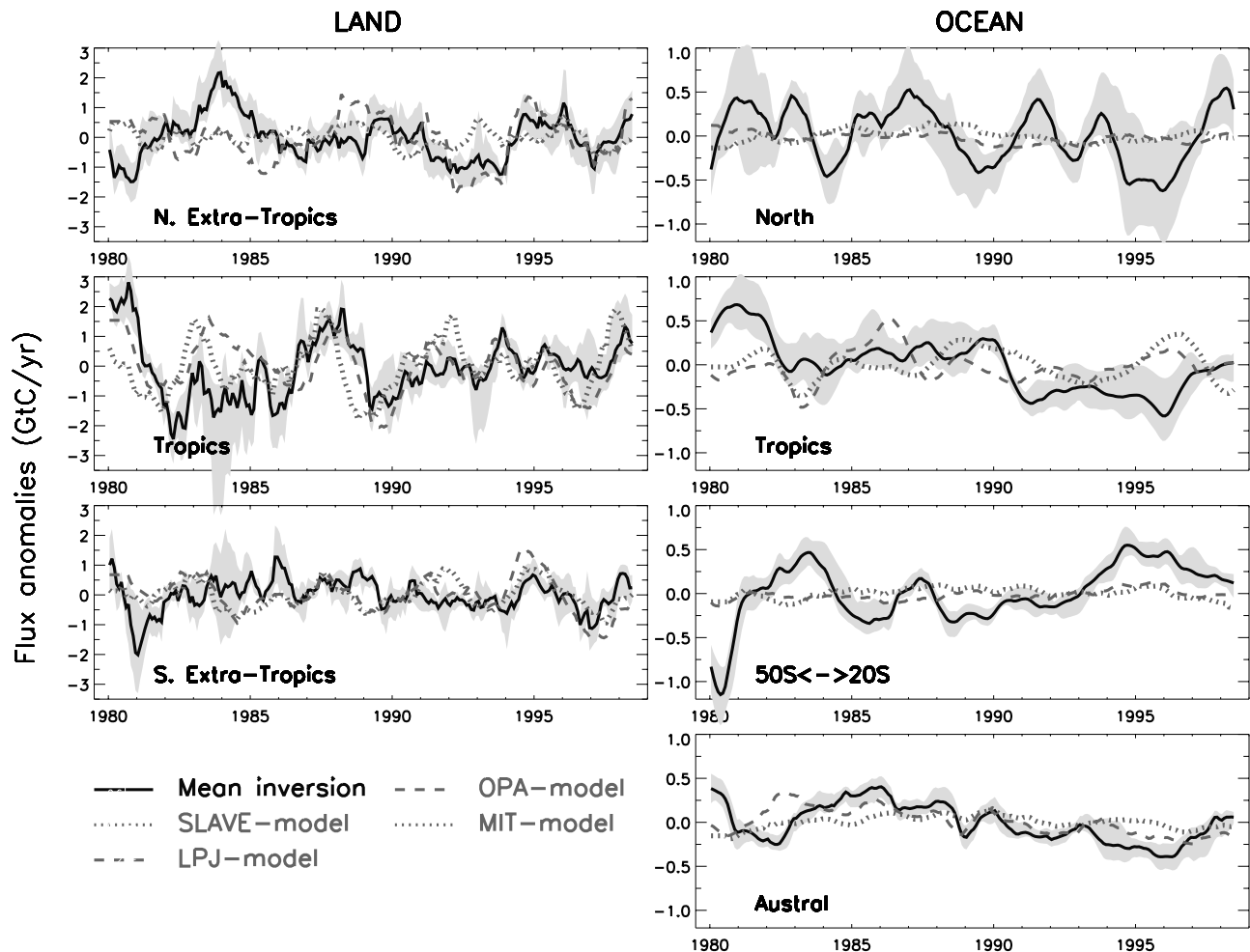
Figure 3. Regional land and ocean flux anomalies over 1980–1998 (in GtC per year) for the Northern extratropical land and ocean (>20°N), the tropical land and ocean, the southern extratropical land (<20°S), the temperate Southern Ocean (50°S–20°S), and the austral ocean. Gray zone and color lines correspond to the different estimates as in Figure 2. See color version of this figure at back of this issue.

same order of magnitude, the latter two having the smallest IAV. A closer look at our ensemble of inversions (gray zone) shows that the inversion for which we have multiplied the errors on the observations by a factor of 2 presents the smallest ocean flux IAV with only a slight reduction of the land flux IAV, a result in closer agreement with the other approaches. Reducing the error on the data directly increases the ocean IAV, as a better fit for nearly two thirds of the stations is required ("marine network"). The optimal error level is, however, difficult to assess, and one might argue that current "marine network" could bias the partition of the flux anomalies toward the ocean fluxes. Moreover, the use of relatively large ocean regions (11) is a potential source of errors ("aggregation error" [*Kaminski et al.*, 2001]) that could also bias the partition of the flux IAV between land and ocean [*McKinley et al.*, 2003].

3.2. Latitudinal Fluxes

[20] We now discuss the flux anomalies by latitudinal bands; three for the land: northern extratropics (>20°N),

tropics, and southern extratropics (<20°S); and four for the ocean: with the southern extratropics split into a 50°S–20°S and an austral region south of 50°S (Figure 3). At this scale, we will not present "Rayner-inv" inversion because (1) their estimates correspond to different regions than ours (north-south and east-west boundaries differ), which prevents a rigorous comparison, and (2) they choose to assimilate only the sites that were available during the entire period (12), which can be seen as a limitation for an indepth discussion of the results at the regional level. As a first remark when downscaling global results, one must consider that the number of atmospheric stations was under 25 before 1985. This does not allow much confidence in the regional results for the early 1980s. We will thus focus on the period 1985–1998. The mean flux IAV over this period (standard deviation) is reported in Table 3 for all regions.

[21] After 1985, land flux variability is dominated by the exchanges with tropical ecosystems (±1.5 GtC yr⁻¹) and the Northern Hemisphere ecosystem (±0.7 GtC yr⁻¹) (Figure 3). More precisely, the 1987–1988 El Niño induces

Table 3. Mean Internal Errors (Estimated by the Inverse Procedure) on the Interannual Flux Variability (IAV), Mean External Errors (From the Ensemble of Inversion) on the IAV, Maximum Internal Correlations Between Any Given Region and the Other Regions of the Table (Value and, in Parentheses, the Index of the Region), and Mean Amplitude of the IAV[a]

Region		Errors		Internal Correlations		IAV	
Name	Index	Internal	External	First	Second	Inverse	LPJ/SLAVE OPA/MIT
NORTHERN HEMISPHERE LAND	1	0.56	0.38	−0.6(2)	−0.6(19)	0.55	0.82/0.34
NORTHERN HEMISPHERE OCE	2	0.38	0.24	−0.6(1)	−0.3(11)	0.32	0.05/0.07
TROPICAL LAND	3	0.98	0.45	−0.3(5)	−0.3(1)	0.71	0.87/0.91
TROPICAL OCE	4	0.27	0.15	0.4(6)	0.3(27)	0.25	0.17/0.18
Southern Hemisphere land	5	0.71	0.32	−0.3(3)	−0.3(22)	0.44	0.79/0.46
SOUTHERN HEMISPHERE OCE	6	0.28	0.10	0.5(25)	0.4(4)	0.19	0.10/0.10
Tundra	7	0.22	0.10	−0.5(13)	−0.3(11)	0.16	0.04/0.01
NORTH AMERICA	8	0.59	0.36	−0.5(11)	−0.4(19)	0.57	0.55/0.24
Boreal North America	9	0.48	0.26	−0.4(21)	−0.4(19)	0.45	0.14/0.04
Temperate North America	10	0.47	0.25	−0.4(9)	−0.2(20)	0.33	0.50/0.24
Eurasia	11	0.57	0.41	−0.5(8)	−0.4(9)	0.37	0.48/0.23
Boreal Europe	12	0.48	0.17	−0.3(13)	−0.2(8)	0.16	0.13/0.07
Boreal Asia	13	0.50	0.23	−0.5(7)	−0.3(15)	0.28	0.15/0.09
Temperate Europe	14	0.38	0.26	−0.2(13)	−0.2(15)	0.33	0.27/0.12
Temperate Asia	15	0.36	0.26	−0.3(13)	−0.2(14)	0.34	0.28/0.10
PACIFIC >20°N	16	0.24	0.15	−0.4(1)	−0.3(11)	0.27	0.05/0.05
Temperate North Pacific	17	0.18	0.11	−0.2(11)	−0.1(1)	0.20	0.04/0.03
North Pacific nord	18	0.17	0.09	−0.3(1)	−0.2(13)	0.11	0.03/0.03
ATLANTIC >20°N	19	0.28	0.15	−0.6(1)	−0.4(8)	0.14	0.03/0.03
Temperate North Atlantic	20	0.24	0.14	−0.3(1)	−0.3(8)	0.10	0.02/0.02
North North Atlantic	21	0.18	0.07	−0.5(1)	−0.4(9)	0.10	0.01/0.02
Tropical America	22	0.81	0.29	−0.4(25)	−0.3(5)	0.44	0.42/0.52
Tropical Africa	23	0.76	0.35	−0.2(5)	−0.2(24)	0.43	0.39/0.30
Tropical Asia	24	0.53	0.40	−0.3(1)	−0.2(23)	0.60	0.20/0.26
Tropical Pacific	25	0.11	0.10	0.5(6)	0.4(27)	0.14	0.16/0.19
Tropical Atlantic plus Indian oceans	26	0.23	0.12	0.3(6)	0.2(27)	0.28	0.06/0.03
20°S−50°S ocean	27	0.28	0.09	0.4(25)	0.3(4)	0.26	0.06/0.05
Austral ocean	28	0.19	0.08	−0.3(27)	0.1(25)	0.19	0.12/0.06

[a]See text for description of the internal and external errors. All-capital words in first column denote a group of individual regions for which we solve the fluxes. Mean amplitude of the IAV denotes standard deviation of the monthly flux IAV averaged across all seven sensitivity tests. These numbers correspond to the restricted period 1985–1998, and to all individual regions of the inversion or grouping of regions (names in capital). Errors and IAVs are expressed in GtC yr^{-1}.

a positive flux anomaly in the tropics not visible in the extratropics, while for the 1997–1998 event the response is more spread between the different latitude bands. Note that the 12-month running mean applied to remove the seasonal cycle extends the duration of the flux changes (i.e., the flux anomaly in the tropics increases in early 1987 whereas the actual El Niño begins only at the end of 1987). During the 1990–1995 period, the northern extratropical land carbon exchange slightly dominates in the inverse results and presents an enhanced uptake after the Pinatubo eruption in 1991 (1 GtC yr^{-1} of increase) and a recovering period in 1994.

[22] The phase and the amplitude of the top-down and bottom-up approaches agree surprisingly well, especially with the LPJ model. The standard deviations of the flux IAV (Table 3) are rather similar for the tropics but slightly different for the northern extratropics, SLAVE model having the smallest variability and LPJ the largest (0.34 and 0.82, respectively, compared to 0.55 for the inversions). The correlation coefficient between the mean inversion and LPJ model is on the order of 0.6 both for the tropical and the northern extratropical ecosystems. With the SLAVE model it only reaches such value for the tropics and only if we account for a 5-month negative lag of that model. Overall the convergence between the inverse approaches and the LPJ biogeochemical model for the tropics and

northern extratropics can be viewed as an encouraging feature that will be discussed in section 4. For the southern extratropical land flux anomaly, the agreement between the two approaches starts in the early 1990s. However, the LPJ flux IAV presents an anomalous uptake between 1994 and 1997 up to 3 GtC yr^{-1} (linked to biomass burning), a decrease much smaller for the inverse or the SLAVE model estimates.

[23] For the ocean, the fluxes estimated from the inversions show interannual variations (±0.5 GtC yr^{-1}) much smaller than for the land, the largest variations occurring for the northern extratropical basins while the fluctuations for the austral ocean basin (south of 50°S) are much smaller (Figure 3 and Table 3). Correlations between the inverse estimates and the SOI index are relatively small for such latitudinal breakdown (even with a possible lag of ±12 months) and the largest anticorrelation, −0.43, is for the northern oceans. If we compare top-down and bottom-up approaches, the agreement is less convincing than for the land, and only the austral ocean, the most homogeneous region, shows some similarities. The inversions and the OPA model produce a similar increase of the austral ocean carbon sink (same trend on the order of −0.5 GtC between 1985 and 1995) with a relatively good agreement for the phase of the IAV (correlation of 0.6) and comparable amplitude (standard deviation of 0.19 and 0.12, respectively). Note
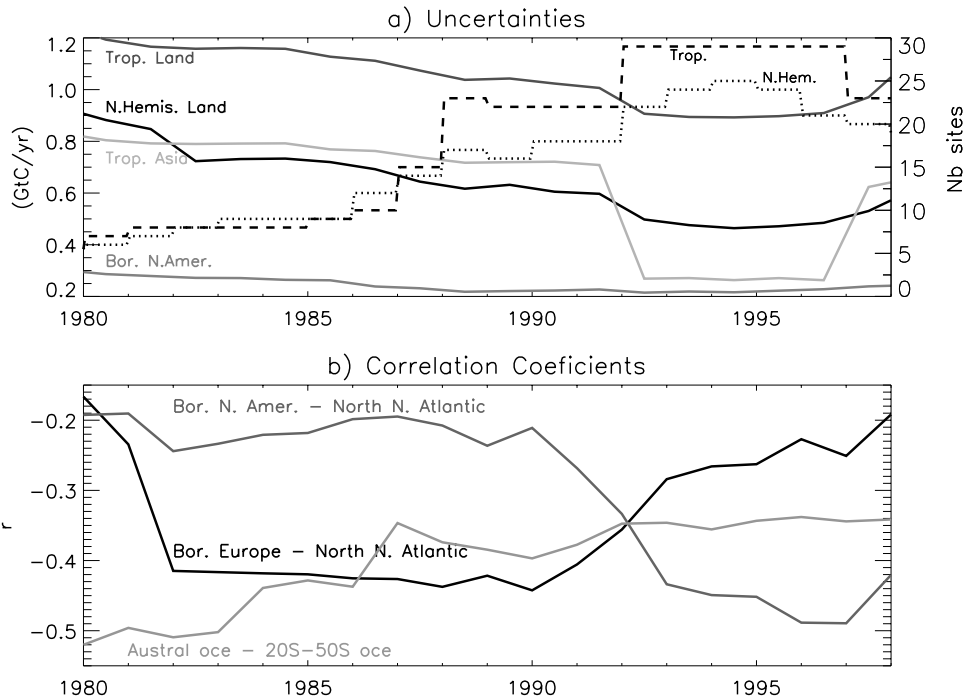
Figure 4. (a) Time evolution of the internal errors (i.e., returned by the inversion) of the flux IAV in GtC yr^{-1} (see text for definition). Mean values from the ensemble of inversion are represented for Northern Hemisphere land and tropical land, as well as for two specific regions, tropical Asia and boreal North America. The dotted and dashed lines represent, shown on the right axis, the number of stations north of 30°N and in the tropics, respectively, as a function of time. (b) Examples of the time evolution of internal correlations (i.e., returned by the inversion) between different regions; temperate with boreal North American; boreal North America with North Atlantic; and boreal European land with North Atlantic.

that the MIT model shows no such trend, as we had to remove it from the initial fluxes (to address model drift). In the tropics, all approaches produce similar amplitude of the flux IAV, but the bottom-up and top-down are not in phase and the inversion does not show as clear a correlation with El Niño events as do the ocean models. However, the agreement is much better when considering the equatorial Pacific Ocean alone. For nontropical oceans, inversions produce much more variability than both the ocean biogeochemical models. Such controversial results will be discussed in section 4.

3.3. Uncertainties in the Inverse Estimates

[24] The synthesis inversion allows estimation of not only the fluxes but their associated error variance-covariance matrix P ("internal error"). These errors only account for the random errors due to the assumed random uncertainties in the observations. From P, we derived an internal error on the flux IAV only (P'; see Appendix C). We also use the spread of the seven sensitivity tests that we performed to partly estimate systematic errors from the standard deviation of the seven flux anomalies ("external error"). Both errors are reported in Table 3 (mean value), and Figure 4a shows the temporal evolution of the internal error for a few regions.

[25] On average, internal errors are smaller for the ocean than for the land regions (marine network), and largest for tropical land (least constrained region). They slightly

decrease in time as the number of stations increases (Figure 4a, left axes). Note the large drop for tropical Asia with the appearance of the South China Sea Cruses in 1992 and conversely with their disappearance in 1998. The external errors are smaller by nearly a factor of 2 than the internal errors, except for the tropical Pacific Ocean (this region has the largest number of sites (ship measurements), which in turn produces a small internal error). This might indicate that the random error in the flux estimate dominates in comparison to the potential systematic errors (i.e., transport model biases) or that the seven sensitivity tests only explore a part of the possible systematic errors.

[26] The robustness of the flux IAVs should be discussed in the light of these uncertainties. At the latitudinal scale, the ratios between the mean amplitude of the IAV and the internal/external errors are close to one/two (Table 3). At the regional scale, these ratios can be significantly lower for particular regions (boreal Europe and Asia), although they remain stable for most oceanic regions and tropical Asia. The large internal errors suggest that we still need more data to statistically assess the IAV signal, and the favorable ratio with the external error suggests that the IAV signal is relatively robust and less subject to systematic errors. This latter result, detailed in Appendix C, supports the conjecture that IAV is better constrained than long-term net fluxes.
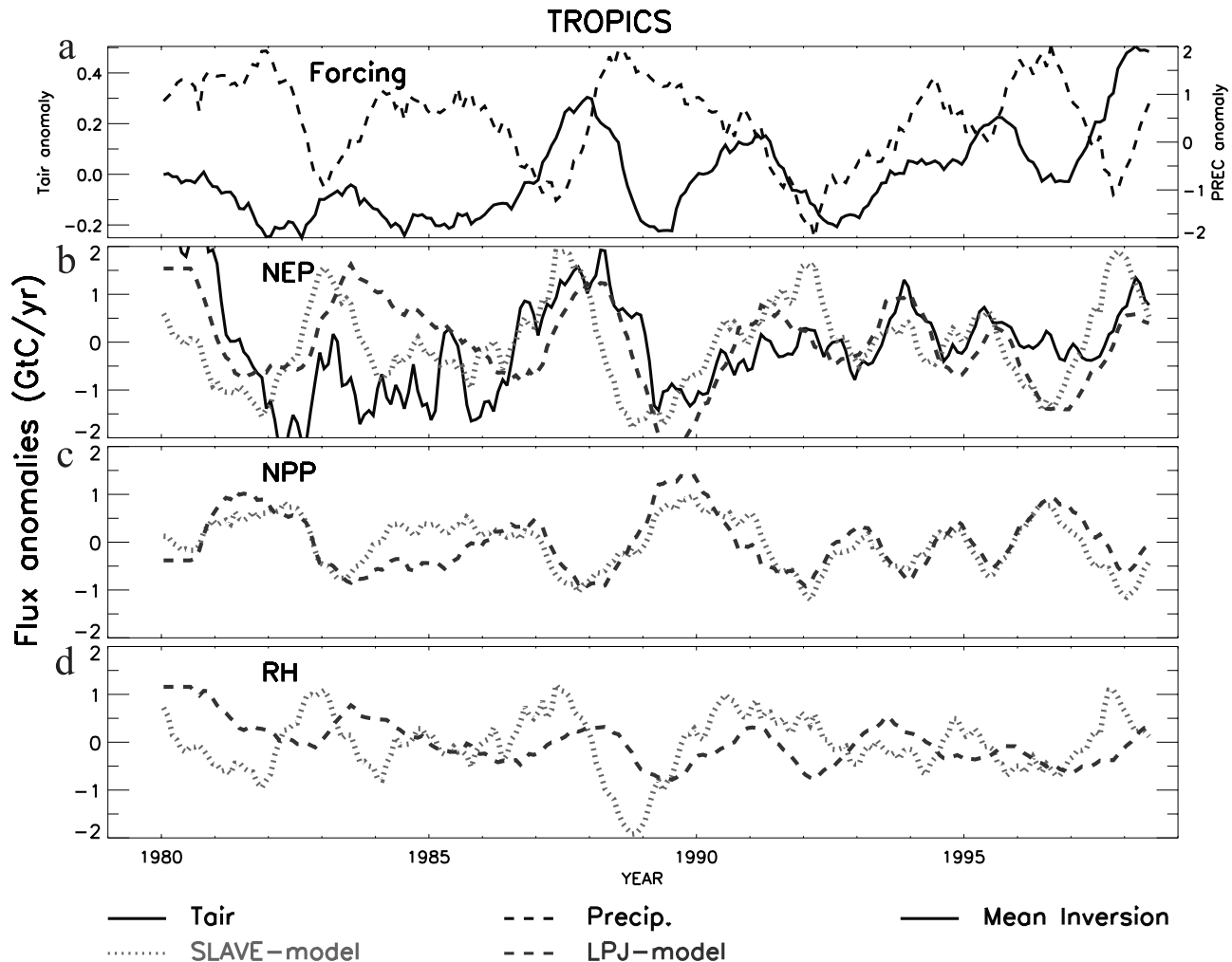
Figure 5. (a) Mean temperature and precipitation anomalies over the tropics for the 1980–1998 period. (b, c, d) Net ecosystem production (NEP), net primary production (NPP), and heterotrophic respiration (RH), respectively, expressed as flux anomalies for LPJ and SLAVE land models. The NEP derived from the inversions (mean value) is overplotted.

[27] Following this idea, one should also stress the potential source of misinterpretation from using only 1 year of wind as explained by *Rödenbeck et al.* [2003]. We partly accounted for such bias, with an additional test using proper winds for each year in a forward mode and inverting for residuals linked to transport IAV (see Appendix C). As a main result, flux IAV is only modified at the regional scale: significantly for the amplitude and slightly for the phase.

[28] Finally, we computed the correlation coefficients between the internal errors. These correlations are on average quite low (absolute value <0.6; see Table 3) and lower than those for the net flux errors reported by *Peylin et al.* [2002]. This is especially true for tropical land and tropical oceans where flux anomalies seem to be more separable than mean fluxes. The time evolution of these correlations, illustrated in Figure 4b, is sometime counter intuitive and may increase as more stations appear (see Appendix C). Overall, one should use some caution to interpret flux IAVs at the regional level where the uncertainties remain large.

4. Discussion

[29] In this section, we assess the biogeochemical factors that control the IAV, with a detailed analysis of the bottom-up models.

4.1. Land Fluxes

[30] Global Net Ecosystem Production (NEP) variability is mainly driven by precipitation for SLAVE model and a combination of precipitation and temperature for LPJ. These global features, however, combine the variability of net primary production (NPP) and heterotrophic respiration (Rh) (including biomass burning for LPJ) which will be discussed individually for two large regions, the tropics and Southern Hemisphere, and the northern extratropics. Additional simulations of the biogeochemical models which

explicitly quantify the relative role of the major climatological forcing (temperature versus precipitation) are included to support the analysis.

4.1.1. Tropical and Southern Hemisphere Fluxes

[31] Precipitation controls NEP variability in the tropics and Southern Hemisphere in both land models. In the tropics, IAV has similar amplitude in both models (Figure 5), with positive anomalies of NEP (larger flux toward the atmosphere) during the El Niño years (1982–1983, 1987–1988, 1997–1998) consistent with the inversion results. In the Southern Hemisphere, the large shift from anomalous source to sink in LPJ between 1995 and 1997 (Figure 3) is due to a decrease in the biomass burning source in response to a large precipitation anomaly.

[32] For these regions, both LPJ and SLAVE show a large positive correlation between NPP and precipitation (0.73 and 0.62, respectively, but with a 4-month positive lag of NPP; see Figure 5). Also, models show a significant negative correlation of NPP IAV with temperature, albeit small relative to that with precipitation. The 1997 and 1998 El Niño years are the exception where the reduction in NPP is equally explained by a reduction in precipitation and by a large positive temperature anomaly. Overall, both models simulate a reduction in tropical NPP during El Niño years on the order of 1–1.5 GtC.

[33] In the tropics during El Niño years, SLAVE simulates an increase in Rh of 1–1.5 GtC whereas LPJ produces a smaller increase of 1 GtC (Figure 5d). The two models show quite different responses of Rh to the climate forcing. SLAVE has a strong anticorrelation (−0.68) with precipitation anomalies whereas LPJ is insensitive (positive correlation of 0.18). As opposed to LPJ, SLAVE includes an inhibition of the decomposition rate at high moisture levels (see equations (B8) in Appendix B1). In the tropics, where moisture levels are high on average, negative anomalies of precipitation could thus lead to an increase in Rh. We performed an additional simulation with SLAVE where the inhibition was removed and found a much better agreement on tropical NEP between the two models (not shown). Regarding Rh sensitivity to temperature, the two models are very similar in the tropics and the Southern Hemisphere.

[34] In addition to NPP and Rh, LPJ simulates natural biomass burning, which tends to increase modeled NEP IAV (except post-Pinatubo years 1992 and 1993), especially during the middle to late 1990s. Biomass burning is anticorrelated with precipitation, reinforcing the land NPP driven response to ENSO. Modeled global IAV in natural biomass burning agrees with *Langenfelds et al.* [2002] and *Duncan et al.* [2003] in predicting maxima and minima emissions in years 1994/1995 and 1995/1996, respectively. Extremely high emissions in 1997/1998, largely associated with fires in southeast Asia [*van der Werf et al.*, 2003], are not captured by LPJ. However, these emissions are in part due to peat fires [*Page et al.*, 2002] and the increased susceptibility of tropical forests to fire due to logging practice [*Siegert et al.*, 2001], both of which are not explicitly modeled in LPJ.

[35] Biomass burning anomalies act in the same direction as Rh anomalies, amplifying the respiration IAV in the tropics and Southern Hemisphere, with an exception for years between 1994 and 1998 in the Southern Hemisphere. This period is characterized by large fluctuations in precipitation with minimum in 1995 followed by a maximum in 1997. While Rh is relatively unresponsive, biomass burning varies by over 1 GtC during this period, and contributes to the large net biosphere anormal release in 1995 in the Southern Hemisphere, followed by uptake in 1997 as simulated by LPJ (Figure 3).

[36] Overall, the differences between SLAVE and LPJ heterotrophic respirations explain most of their NEP differences. The phase of the NEP anomalies, especially during the 1982–1983 and 1987–1988 El Niño years, shows a positive lag in SLAVE compared to LPJ of close to 8 months. Although the inversion estimates are more in line with LPJ results, neither Rh formulation can be strongly recommended at this stage.

4.1.2. Northern Hemisphere Flux

[37] Although smaller than in the tropics, the flux IAV in northern extratropics is substantial and different among biospheric models. IAV is driven by temperature in LPJ but not in SLAVE. Models differ primarily in their respiration response to climate variability, their NPP responses being comparable (Figure 6). In SLAVE, Rh is almost insensitive to temperature variability (correlation 0.23) whereas LPJ shows a strong positive correlation (0.86). Formulations relating Rh to temperature differ among models with SLAVE adopting a "Q10" approach, and LPJ the "Lloyd and Taylor" (modified Arrhenius) equation (equation (B3) in Appendix B1). At low temperatures the "Lloyd and Taylor" formulation is more sensitive to a unit change in temperature, and visa versa at high temperatures. For example, a unit increase in temperature around a mean of 5°C results in an increasing respiration rate of 7% and 12% for SLAVE and LPJ, respectively, with an approximately equal response around a mean temperature of 25°C. This explains the differential response between the two models with respect to Rh in temperate and boreal regions.

[38] During the "post-Pinatubo" period, the mean atmospheric CO$_2$ growth rate was relatively low during 1991–1993 and recovered in 1994–1995. The observed cooling of ~0.6°C between late 1991 and mid-1992 (Figure 6a) drove a decrease of Rh in LPJ only. When the Rh of the SLAVE model is computed using the "Lloyd and Taylor" instead of its standard "Q10" formulation, Rh decreased in 1992 in phase with LPJ but with only half its amplitude (simulation results not shown). Between 1988 and 1992, both models show increasing biospheric uptake due to the positive response of NPP to an increase in precipitation, in agreement with the recent findings of *Nemani et al.* [2002] for the United States. However, LPJ simulates a maximum of NPP in 1992 before a reduction in 1993, whereas SLAVE only simulates the reduction. The combination of the larger Rh reduction in LPJ compared to SLAVE and the peak of NPP in LPJ explains the LPJ net biospheric negative anomaly following the Pinatubo eruption (Figure 6).

[39] A different explanation has been proposed which explains the post-Pinatubo anomalous sink by the effect of enhanced diffuse radiation on canopy photosynthesis after the Pinatubo eruption [*Farquhar and Roderick*,
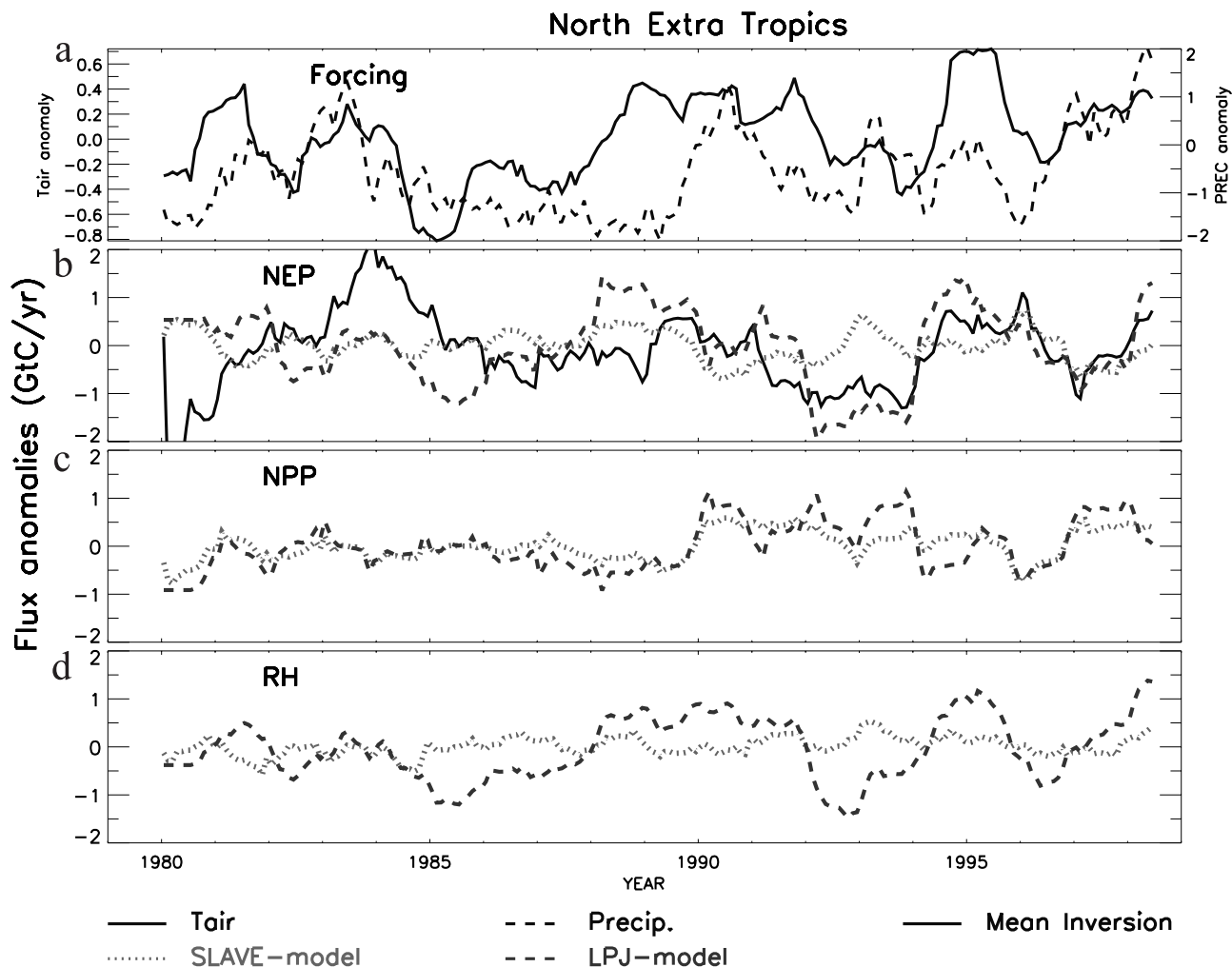
Figure 6. Same as Figure 5, but for the northern extratropics.

2003; *Gu et al.*, 2003]. To assess the validity of this hypothesis using atmospheric observations, one would need information on the IAV of the gross fluxes based on satellite observations or atmospheric tracers such as the ¹⁸O/¹⁶O ratio in CO₂ [*Ciais et al.*, 1997].

[40] As discussed by *Bousquet et al.* [2000], the inversion supports the large negative anomaly in 1992–1993 over the Northern Hemisphere estimated by LPJ (Figure 6). However, the inversion essentially locates this anomaly in North America (Figure 7), whereas LPJ simulates also a smaller but significant uptake anomaly in Eurasia.

[41] The inversion result attribute an enhanced North America sink to an increase of the mean atmospheric concentration difference between Atlantic and Pacific sites [*Bousquet et al.*, 2000, Figure 4] in 1992–1993. To investigate the robustness of this anomaly, we carried out several additional sensitivity inversions. First, trying to account for interannual variations of the transport (Appendix A) leads to a larger sink in 1992–1994 (curve "Mean_inv + wind"; Figure 7). Second, to test if such anomaly is an artifact linked to the appearance of new sites in 1992–1994, we performed two inversions: one where we stopped assimi-

lating new sites after 1990 ("stat before 90"), and one where we used extrapolated data from GLOBALVIEW for all 68 sites over the 1980–1998 period ("stat. interpol."). Although still present, the negative anomaly in the "stat before 90" inversion is smaller by a factor of 2, which confirms the importance of having new sites like MHD, ICE, and ITN in 1992–1993 to fully separate flux anomalies between the Northern Hemisphere regions. The "stat. interpol." inversion with an anomaly comparable to the mean inversion anomaly confirms that it is unlikely to be an artifact linked to the relative position (i.e., mean concentration) of those sites. Overall, the large North American anomalous sink in 1992–1993 estimated by the inversions seems to be robust to the use of available observations, and is supported by LPJ's results.

4.2. Ocean Fluxes

[42] IAV in air-sea fluxes is driven by changes in the partial pressure of surface water CO₂ (pCO₂) and in gas exchange. Gas exchange is mainly a function of wind speed. The pCO₂ combines the impact of temperature on carbon solubility, and of physical transport and marine biological
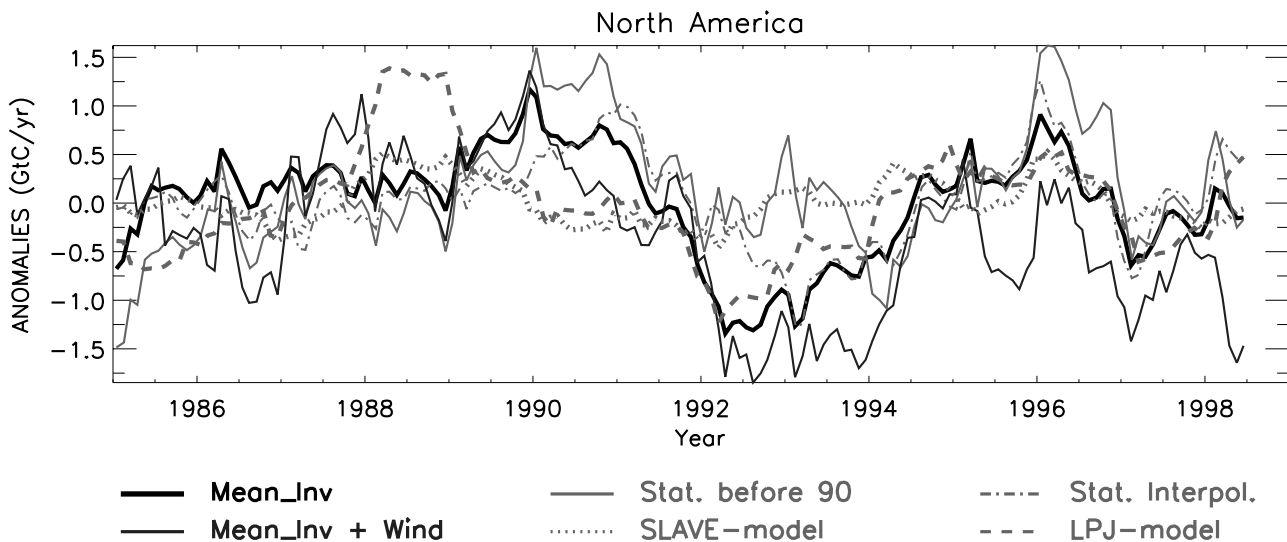
Figure 7. Flux IAV estimated for North America (three individual regions of Figure 1 grouped together) for different inverse setup and for bottom-up models: mean inversion (black), inversion where we stop assimilating new stations after 1989 (dark blue), inversion with all 67 sites extrapolated over the entire period (1980–1998) from Globalview (orange), and mean inversion plus some corrections computed from the interannual wind experiment (i.e., inversion of the concentration differences from a direct simulation with and without interannual winds; see section 3.3; light blue). See color version of this figure at back of this issue.

export on dissolved inorganic carbon (DIC). We discuss these processes for the equatorial Pacific, Austral, and Northern oceans.

4.2.1. Equatorial Pacific

[43] As a result of repeated equatorial Pacific-wide surveys of sea-surface pCO$_2$, the impact of El Niño/Southern Oscillation (ENSO, captured by the Southern Oscillation Index, SOI) on the air-sea CO$_2$ fluxes is well established [*Feely et al.*, 1999]. The normal outgassing of CO$_2$ in this region is reduced by up to +0.5 GtC yr^{-1} during El Niño events (1982–1983, 1986–1987, and 1997–1998) and conversely during La Niña conditions (1984–1985, 1988–1989) (see Figure 8).

[44] The inversion and ocean models are in excellent agreement with the observed variations in terms of magnitude, but there remain some phase differences particularly associated with the OPA model. At the peak of the 1986–1987 El Niño, for example, the OPA model lags the inversion results by nearly 1 year [see also *Bousquet et al.*, 2000]. Replacing the climatological winds with interannually varying winds ("mean + wind" curve, Figure 8) in the atmospheric inversion only reconciles some of the phase differences in the early 1980s. The phasing and the magnitude of the IAVs simulated by MIT model tend to be more similar to the inversion results and are generally in good agreement with the observations.

[45] In both models, ENSO alters the air-sea CO$_2$ flux by changing the slope of the thermocline and upwelling, thereby changing the vertical supply of DIC to the surface, in agreement with observations [*Archer et al.*, 1996]. This upwelling effect more than overrides the counteracting effect of the changes in SST and biological export, both of which would tend to increase the CO$_2$ outgassing during El Niño events, the former because of

the higher than normal SSTs and the latter because of reduced nutrient supply. *McKinley et al.* [2004] also find that wind speed variability and change in the longitudinal displacement of the western warm pool contributes to the flux IAV.

[46] Differences between the MIT model and the OPA model in the equatorial Pacific are caused by differences in the mean state of the ocean and in the parameterization of marine export production. The MIT model has a surface to depth gradient of DIC that is underestimated by ∼25% compared to the observations of *Goyet et al.* [1999], which may reduce variability, while the OPA model captures this gradient quite well. The OPA model shows variations in surface chlorophyll that are overestimated by 1.5 compared to satellite observations, while the simplified export parameterization of the MIT model tends to damp export flux variability. Further, the variability of export production in the OPA model increases over the course of the run, which increasingly damps the OPA CO$_2$ flux variability signal with time.

[47] Despite these differences, the agreement between the ocean models, the atmospheric inversions, and the in situ observations for the equatorial Pacific is remarkable. There is less agreement between the bottom-up and top-down approaches in the other tropical ocean regions, so that the comparison for the tropical oceans as a whole is worse (Figure 3).

4.2.2. Austral Ocean

[48] In the austral ocean, both the inversion and the OPA model show a constant increase in air-sea CO$_2$ flux since 1984 (Figure 3). Results from the MIT model are not compared here as long-term trends were removed (see section 2.3). No direct observations of flux IAVs are available for this region.
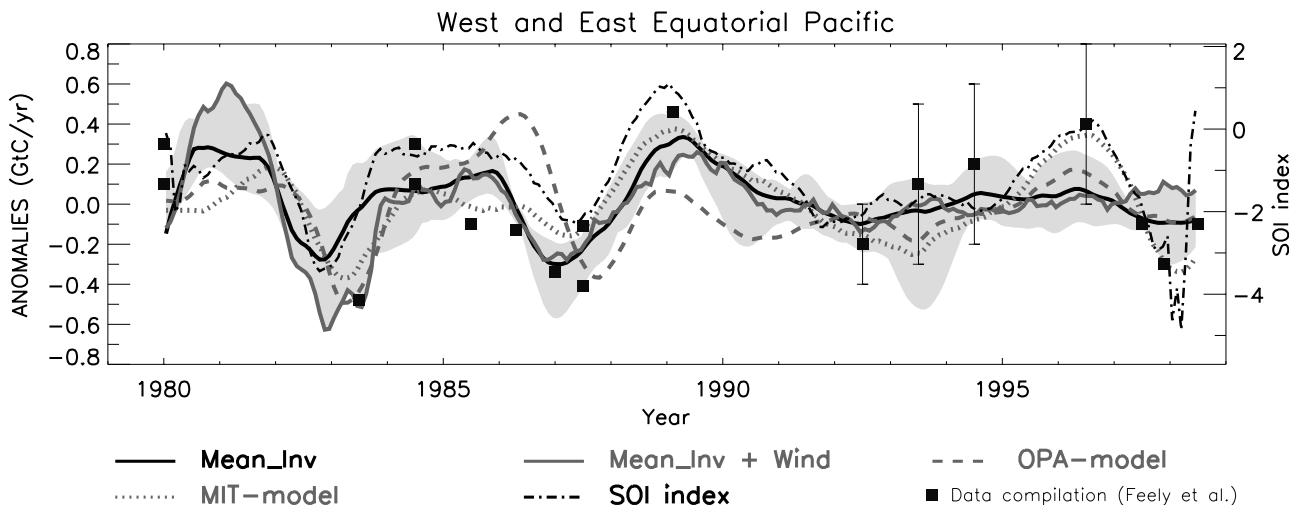
Figure 8. Flux anomalies for the equatorial Pacific Ocean from our ensemble of inversions (gray zone for the full range and dark line for the mean), from the mean inversion plus some corrections computed from the interannual wind experiment (i.e., inversion of the concentration differences from a direct simulation with and without interannual winds; see section 3.3), from the OPA and MIT ocean models, and from a compilation of oceanic data [*Feely et al.*, 1999]. The SOI index is overplotted (right axis). See color version of this figure at back of this issue.

[49] In OPA, changes in DIC driven by changes in physical transport dominate the variations in CO₂ flux (Figure 9; see *Le Quéré et al.* [2000] for a description of the equations). OPA simulates interannual variations in the mean mixed layer depth of up to ±8 m. When the mixed layer depth deepens, waters rich in DIC are entrained into the surface and CO₂ outgasses to the atmosphere. The magnitude of this effect is similar in amplitude and in phase with the contribution of DIC to the total sea-air CO₂ flux (Figure 9). In comparison, the trend in the ocean sink caused by the increase in atmospheric CO₂ is estimated at ∼0.3 PgC per decade [*Le Quéré et al.*, 2003b], about half of the trend produced by the OPA model and by the inversion in the Southern Ocean only. Thus this trend appears to be caused by changes in ocean stratification.

[50] The year-to-year variations in mixing depth are mostly caused by local variations of ±10 to ±60 m in the Pacific sector of the austral ocean, associated with the passage of the Antarctic Circumpolar Wave (ACW). The ACW is a perturbation of SST, ice extent and surface wind that was observed to propagate around the austral ocean [*White and Peterson*, 1996]. The perturbations affect ocean biogeochemistry in a way that has been modeled [*Le Quéré et al.*, 2000] but never evaluated due to the lack of time series observations in this region of the world. Our study suggests that atmospheric observations may be useful for this purpose. However, in the current configuration of the atmospheric inversion, the austral ocean appears as one region, and thus it is not possible to separate east-west variations to clearly identify the role of the ACW.

[51] Climate models consistently predict a major stratification of the ocean surface with global warming [*Sarmiento et al.*, 1998]. Our comparison suggests that the natural CO₂ sink in this region would increase by 0.05 to 0.1 GtC yr⁻¹ for every meter of stratification of the austral ocean. However, stratification also stops anthropogenic CO₂ from

penetrating to the intermediate and deep waters. Over the 1980–1998 period, the impact of stratification on CO₂ fluxes is dominated by natural processes. Over a longer time period, however, models suggest that the effect of stratification on anthropogenic CO₂ dominates and that the CO₂ sink in the austral ocean is reduced [*Sarmiento et al.*, 1998].

4.2.3. North Atlantic and North Pacific

[52] Over the entire North Atlantic and North Pacific combined, the inversion suggests variations of CO₂ fluxes up to ±0.5 GtC yr⁻¹, whereas the ocean models find variations of only up to ±0.2 GtC yr⁻¹ (Figure 3). Over the North Atlantic, the inversion suggests interannual variability in the fluxes of more than ±1 mol/m²/yr (Figure 10), which, assuming little change in the gas exchange coefficient, would require interannual anomalies in the ocean pCO₂ of more than ±15 ppm. Such variability should be visible in oceanic pCO₂ measurements.

[53] Long time-series observations of oceanic pCO₂ exist at the subtropical North Atlantic (Bermuda Atlantic Time-series Study, BATS) and Pacific (Hawaii Ocean Time-series, HOT) [*Bates et al.*, 2002; *Gruber et al.*, 2002; *Karl and Lukas*, 1996; *Winn et al.*, 1998]. At these stations, IAV in the oceanic pCO₂ varies by 10 ppm only, and is mainly controlled by anomalies in SSTs with some compensatory effects by anticorrelated changes in DIC [*Bates et al.*, 2002; *Gruber et al.*, 2002]. However, there exists a significant inverse correlation between SST anomalies and wind speed at both sites, so that colder than normal years with lower than normal oceanic pCO₂ tend to have higher wind speeds and hence higher gas transfer coefficients leading to interannual flux variability of up to ±0.8 mol/m²/yr at both sites [*Gruber et al.*, 2002]. A surprising finding is that the Bermuda-based interannual flux variability estimates (if projected over the whole North Atlantic) not only agree with the inversion-based estimates in terms of magnitude,
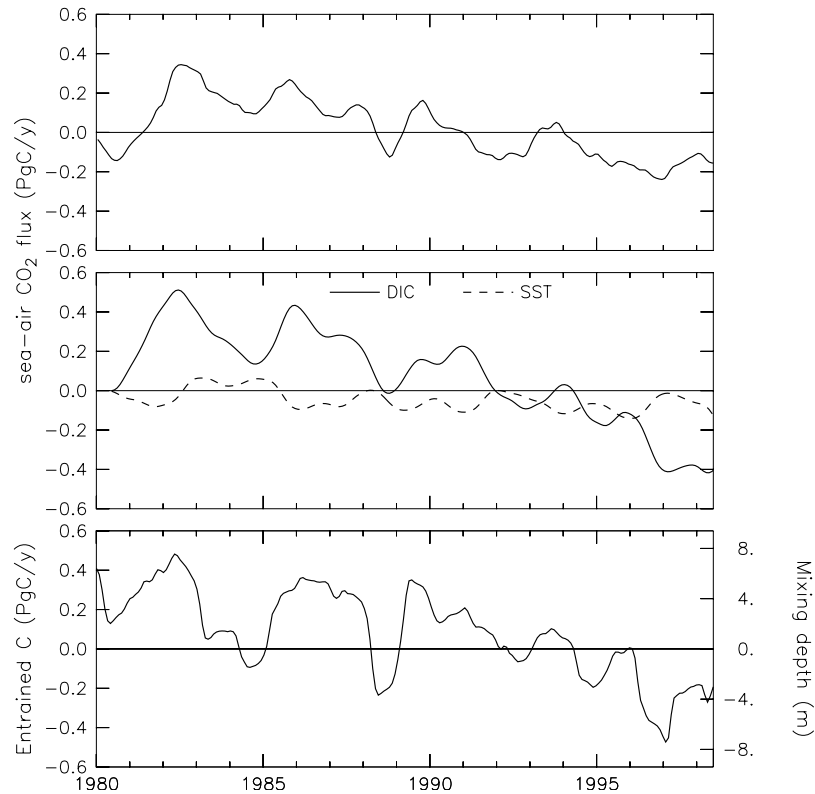
Figure 9. (top) Sea-air CO$_2$ flux in the Southern Ocean (PgC/yr) computed using the OPA ocean model. (middle) Individual contributions of dissolved inorganic (DIC) and sea surface temperature (SST) to the total sea-air CO$_2$ flux shown in the top panel. The differences between the sum of the DIC and SST contribution and the curve of the top panel are caused by the contribution of alkalinity and by interannual variations in gas exchange. (bottom) Changes in the mixing depth (right axis) and the associated entrainment of total carbon at the surface by vertical mixing. The amount of entrained carbon is computed by estimating the impact of mixing intermediate waters with rich DIC on surface ocean pCO2, and multiplying by an average gas exchange.

but also in phase [*Gruber et al.*, 2002]. This may indicate that the ocean models substantially underestimate interannual variability in the Northern Hemisphere extratropics.

[54] However, ocean models compare relatively well with observations at BATS and HOT particularly with regard to phasing (Figure 11). To be accurate at the basin scale, models must correctly simulate the processes that control CO$_2$ flux IAV at higher latitudes. The observation that the seasonal cycle of pCO$_2$ switches from being controlled by SST to being controlled by surface ocean DIC at about 40° latitude [*Takahashi et al.*, 2002] suggest that the same may be true of interannual variations. If this is the case, then variations in lateral and vertical mixing and biological export production are primarily responsible for air-sea CO$_2$ flux variations at high northern latitudes, similar to what we found for the Southern Ocean. These relationships are found to hold in the North Atlantic for the MIT model, but not in OPA. In the North Pacific, SST and DIC variations compete in driving the interannual variability of pCO$_2$ in both models [*Le Quéré et al.*, 2003b; *McKinley et al.*, 2004].

[55] Nevertheless, there are two reasons to suggest that the ocean models may underestimate air-sea flux IAV in the

extratropical Northern Hemisphere. First, the ocean models may underestimate physical variability of the oceans. We know that the variability in the ocean dynamics of the OPA model is underestimated at high latitudes [*Le Quéré et al.*, 2000], and the MIT model underestimates sea surface height variability relatively equally at all latitudes. Still, the simulated mixed layer depth variability compares well to observed variations at BATS and HOT in both models. Second, the dynamic, temperature and biological effects on ocean CO$_2$ tend to cancel each other at high latitudes. As each of these individual effects can be on the order of 20–40 ppm, the resulting modeled flux becomes the difference between three large numbers, which is difficult to establish with accuracy.

[56] Alternatively, the atmospheric inversion may be overestimating ocean variability in the North Atlantic and North Pacific. This can be due to the inability of the atmospheric network to fully separate land and ocean fluxes with the result of some land variability leaking into the ocean regions. The relative large anticorrelation between the northern Atlantic region and the Northern Hemisphere land (−0.5, Table 3) illustrates such weakness of the current inversions. A thorough analysis of existing pCO$_2$
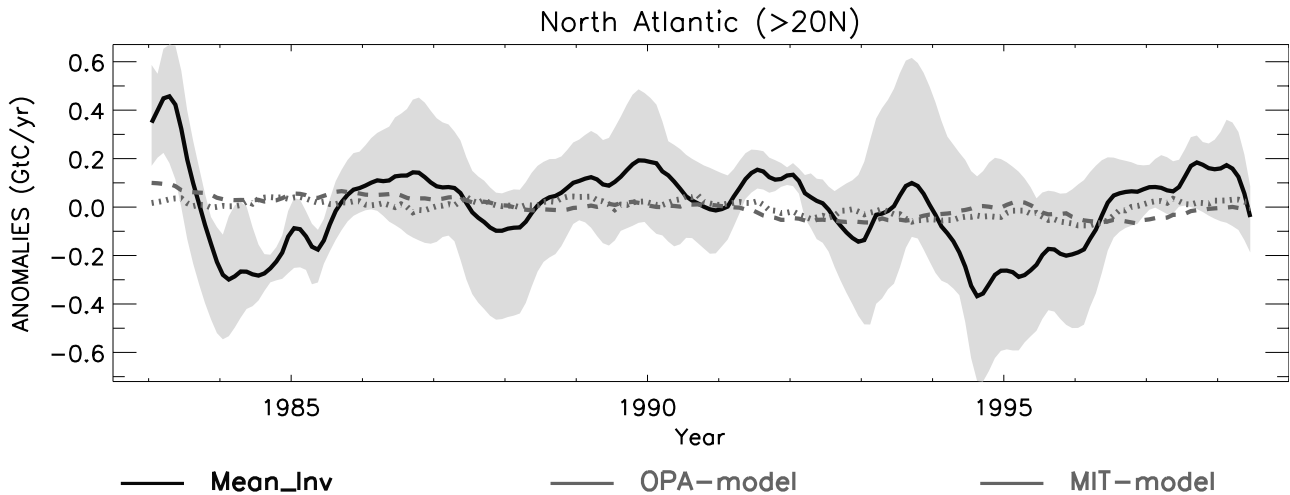
Figure 10. Flux anomalies for the North Atlantic Ocean (north of 20°N) from our ensemble of inversions (gray zone for the full range and dark line for the mean) and from the OPA and MIT ocean models.
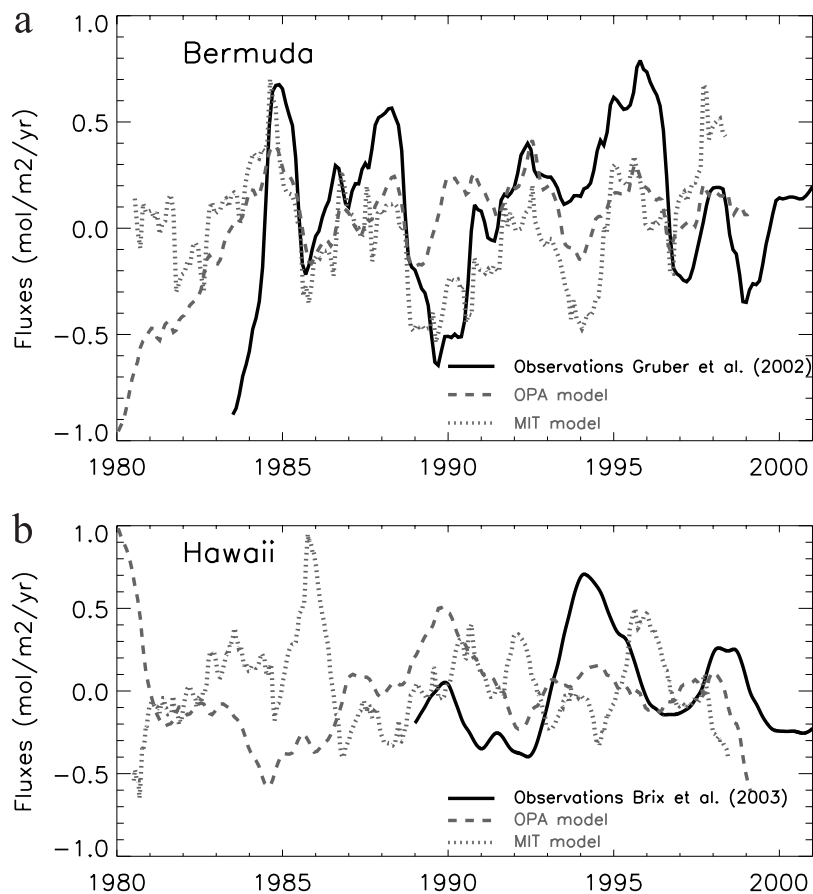

Figure 11. Estimates of air-sea CO$_2$ flux anomalies for (a) the oceanic region near Bermuda (32°N; 64°W) and (b) the oceanic region near Hawaii (22°N; 158°W). The "observed" flux anomalies for Bermuda were estimated by *Gruber et al.* [2002] for station "S"/BATS, and those for Hawaii were estimated by *Brix et al.* [2004] for Station ALOHA. Both estimates are derived from observed surface ocean pCO$_2$ variations and estimated variations in the gas exchange coefficient. For the MIT model, a 3° × 3° region centered around the observing site was used.

measurements in the North Atlantic and Pacific oceans would provide a useful indication on the variability in these regions, and help resolve the discrepancies between the top-down and bottom-up approaches.

5. Summary and Conclusions

[57] We present an intensive comparison of the interannual variations of carbon flux estimated either from a series of inversions (top-down approaches) or from two land (LPJ and SLAVE) or two ocean (OPA and MIT) carbon cycle models (bottom-up approaches). The inversions based on a time-dependent approach use a long record of atmospheric observations covering the 1980–1998 period and two different transport models. Among the large number of global land biosphere models [*Cramer et al.*, 1999, 2001], LPJ can be considered as a sophisticated model of the energy, carbon, and water balance, while SLAVE is a more simplified global carbon model. For the ocean, OPA and MIT models are state-of-the-art models that computed air-sea flux IAV over the period 1980–1998. The major findings of this comparison are as follows:

[58] 1. In agreement with previous studies, atmospheric CO$_2$ variability is dominated by land fluxes. The phase of the CO$_2$ flux anomalies is predominantly controlled by the El Niño/La Niña cycles (relative land source and sink of CO$_2$ to the atmosphere, respectively), with the exception of the post-Pinatubo period in the early 1990s (large land sink).

[59] 2. The inverse estimates agree well with the results of the two land biosphere models (LPJ and SLAVE) at the latitudinal and even regional scales, in terms of both phase and amplitude of the major anomalies.

[60] 3. Both land models agree well for the response of NPP to climate variability.

[61] 4. Major differences between the two land models arise for the response of Rh to precipitation and temperature. The respiration rates for high moisture levels, typical of the tropics, are poorly represented in the models and could significantly change the net flux anomalies. The sensitivity of Rh to low temperature, typical of the northern extratropics, is critical. The "Lloyd and Taylor" formulation of the LPJ model produces much larger variations than that of the SLAVE model (Q10), and leads to net flux anomalies more in line with the atmospheric inversions.

[62] 5. The inverse estimates agree well with the results of the two ocean carbon models (OPA and MIT) in the equatorial Pacific and partly in the Southern Ocean, but results are very different at high latitudes of the Northern Hemisphere.

[63] 6. Both models find that the equatorial Pacific drives the global air-sea CO$_2$ flux variability. This variability is driven by changes in physical processes associated with ENSO, specifically thermocline slope, upwelling, warm pool displacement, and wind speed.

[64] 7. In the Southern Ocean, the inversions and the OPA model produce a similar increase of ∼0.5 PgC/yr in carbon uptake over the 1980–1998 period. In the OPA model, this increase results mainly from the stratification of the upper ocean which isolates carbon-rich deep waters.

[65] 8. In the northern oceans, the inversions produce variability of ±0.5 PgC/yr, much larger than the ±0.2 PgC/yr produced by both models. However, both models reproduce relatively well the observed variations of the time-series stations of BATS and HOT, located at the midlatitudes of the Atlantic and Pacific oceans. Thus the disagreement between the inversions and the models largely comes from the high-latitude oceans.

[66] 9. As noted by *Bousquet et al.* [2000], CO$_2$ flux IAVs are more safely assessed by the inversions than the mean net sources and sinks. Both the internal uncertainties on the IAVs (i.e., random uncertainties associated with data or transport model) and the estimated external uncertainties (i.e., systematic errors from the use of a given transport model) are indeed significantly lower than the mean amplitude of the signal (IAVs) when considering the continental scale.

[67] This study illustrates the benefit of comparing top-down estimates to predictions of process-based carbon models. Rather than the usual direct comparison of the inversions with climatic variables, our approach helps unravel and validate the most critical processes that control land/ocean carbon fluxes. Although the inverse method could be significantly refined (accounting for better prior information, solving for a much larger number of regions to avoid "aggregation errors," using more than two transport models), we believe that the limitations of the current inverse approaches arise mainly from lack of data. In the near future, the potential use of satellite data [*Chedin et al.*, 2003] might be a critical next step. More directly, the use of continuous measurements (more than 20 sites globally) and the information contained in the "synoptic events" will certainly help to resolve more precisely specific sources and sinks of CO$_2$, provided that we will be able to use accurate mesoscale-type models [*Law et al.*, 2003]. Finally, one should keep in mind that the bottom-up approaches still miss processes which could lead to some misinterpretation.

Appendix A: Atmospheric Inverse Set-Ups

[68] We designed a Bayesian synthesis inversion based on work by *Peylin et al.* [1999] and *Bousquet et al.* [2000], solving for monthly fluxes over a "large region." We indeed divided the land surface into 11 regions and the ocean surface into 8 regions for the standard set-up (Figure 1) with regional fluxes being assigned a priori monthly values, monthly uncertainties, and spatial patterns. We calculated the atmospheric CO$_2$ distribution at all stations caused by atmospheric transport acting on a pulsed source of 1 GtC emitted at a constant rate by each region and for each month. The simulations are performed with a 3-D global transport model (TM2 [*Heimann*, 1995]), and we archive the resulting CO$_2$ concentration field for the following 2 years (response functions). The obtained land, ocean, and fossil response functions are then linearly combined, the weight corresponding to the monthly flux magnitude we solve for. Note that fossil emissions are set to fixed monthly values based on interannual fossil fuel emissions statistics [see *Bousquet et al.*, 2000] and that land fluxes comprise fluxes associated with land use and

cover changes and other biospheric sources and sinks. We minimize a cost function which is the sum of both the distance between model responses and observations and the distance between a priori flux estimates and optimized flux estimates, using specific weights (errors).

[69] Additional constraints to limit unrealistic month-to-month fluctuations of the source magnitudes, i.e., variations greater than 200% of the a priori prescribed variations (SIB2 and Takahashi models for land and ocean, respectively), are also employed [*Peylin et al.*, 1999]. We also add a constraint on the global oceanic uptake of 2.0 ± 1.2 GtC yr^{-1} (for each year of the whole period), based on O$_2$/N$_2$ data [*Battle et al.*, 2000]. Finally, we do not model explicitly year-to-year changes in the atmospheric transport over 1980–1998. Analyzed ECMWF winds for year 1990 are recycled to perform the response function calculations. As this hypothesis may lead to bias in monthly flux estimates [*Rödenbeck et al.*, 2003], we performed a sensitivity study to evaluate the impact of interannual meteorology on our results (see section 3.3).

[70] We carried out a series of inversions to investigate the sensitivity of our inverse results to particular components of the inversion (seven major as per *Bousquet et al.* [2000]):

[71] 1. We used the TM3 model instead of TM2 to test the impact of using a different transport parameterization, which was reported to be a main source of uncertainties when inverting mean fluxes [*Gurney et al.*, 2002]. TM3 is based on the same scheme as TM2, but it has a higher vertical and horizontal resolution (72 × 48 × 19 hybrid levels compared to 48 × 25 × 9 sigma levels) which produces a CO$_2$ distribution over continents very different from TM2. In particular, TM3 generates large positive rectification gradients between land and oceans in the Northern Hemisphere, unlike TM2.

[72] 2. We used recycled 1993 meteorological fields instead of 1990 fields to test the impact of using a single year of the atmospheric transport.

[73] 3. We carried out a test inversion with 16 continental and 14 ocean regions to partly evaluate the impact of spatial discretization of prior sources.

[74] 4. We multiplied all errors on the data by an arbitrary factor of 2, as we may underestimate some observational errors (representativeness of stations in the model, data selection, etc.).

[75] 5. We inverted only the 20 sites covering the full 1980–1998 period to study the effect of the appearance of new data in the assimilation scheme.

[76] 6. We removed the additional constraint on the global ocean uptake.

[77] 7. We inverted deseasonalized data at each site instead of monthly seasonal values to test the impact of the seasonal cycle in the results.

[78] We also include in this paper the results of an independent inversion "Rayner-inv" that is different from the above ensemble of inversions in almost every significant respect with different response functions, a different transport model and different data, most notably the use of the long δ^{13}C record from Cape Grim. This inversion is an update of *Rayner et al.* [1999]. The treatment of δ^{13}C is

aimed at using this tracer to constrain interannual variability. Therefore initial values of the disequilibrium and its linear trend are retrieved from the inversion to prevent them polluting net flux estimates. Interannual variations are ascribed, to first order, to net fluxes. However, an anomalous δ^{13}C arising from a net flux anomaly will decay naturally as it is diluted by exchange with underlying reservoirs. This dilution by the gross fluxes is now parameterized in the δ^{13}C response functions with decay constants from *Trudinger et al.* [1999]. Note, however, that this inversion does not treat climatic effects on globally averaged fractionation [*Scholze et al.*, 2003].

Appendix B: Land and Ocean Biogeochemical Models

B1. Land Carbon Models: LPJ and SLAVE

B1.1. LPJ Model

[79] The Lund-Potsdam-Jena Dynamic Global Vegetation Model (LPJ-DGVM [*Sitch et al.*, 2003; *Smith et al.*, 2001] is a process-based biosphere model combining terrestrial vegetation dynamics and biogeochemistry. Modeled processes primarily responsible for the land-atmosphere carbon exchange include plant production, autotrophic respiration, natural biomass burning, and soil and litter decomposition.

[80] Primary production is calculated using the Farquhar photosynthesis model [*Farquhar et al.*, 1980], as generalized by *Collatz et al.* [1991]. Leaf nitrogen and Rubisco activity are assumed to vary both seasonally and with canopy position such as to maximize net assimilation. Net primary production (NPP) is calculated as a function of absorbed photosynthetically active radiation (APAR), itself a function of vegetation cover and phenology, the canopy conductance (gs), air temperature (T), the atmospheric CO$_2$ concentration, the ratio of the intercellular to ambient partial pressures of CO$_2$, and leaf biomass (Cleaf).

[81] Two litter (above and below ground) and two soil pools (fast and slow) are defined. Heterotrophic respiration (Rh) is modeled as a function of litter and soil substrate, tissue-specific base turnover times, temperature, and soil moisture by applying first-order kinetics,

$$dC/dt - C\text{input} = -kC, \tag{B1}$$

$$k = (1/\text{tao10}) \times g(T) \times f(W)/12, \tag{B2}$$

$$g(T) = \exp[308.56((1/56.02) - (1/(T + 46.02)))], \tag{B3}$$

$$f(W) = 0.25 + 0.75 \times W, \tag{B4}$$

where C represents the carbon content in a given substrate pool, *C*input is the carbon input from tissue turnover and litter decomposition into the litter and soils pools, respectively, and tao10 is the turnover time of the litter (2.86 years), fast soil (33.3 years), and slow soil pools (1000 years) at 10°C [*Meentemeyer*, 1978]. The temperature dependence $g(T)$ follows the modified Arrhenius relation-

ship [*Lloyd and Taylor*, 1994], with decomposition of the belowground litter and soil pools dependent on soil temperature, and aboveground litter on air temperature. An empirical soil moisture relationship from *Foley* [1995] is adopted, $f(W)$, where $W(m)$ is the average moisture status in the upper soil layer in month m.

[82] Natural biomass burning is modeled as the combination of fire occurrence and its effects [*Thonicke et al.*, 2001]. Fire occurrence depends on fuel load and litter moisture, both of which are influenced by climate and vegetation. The length of the fire season is translated into an area burnt, and vegetation mortality within that area (therefore the biomass burning flux) depends on PFT-specific fire resistances. For this study, annual natural biomass burning fluxes are weighted by the seasonality of Rh to produce seasonal fluxes, which are then added to the Rh fluxes.

B1.2. SLAVE Model

[83] The SLAVE model is a terrestrial carbon model that simulates for 10 vegetation types the net primary productivity, the allocation of carbon within the plant, and the growth and decay of living biomass. It also simulates litter and soil carbon cycle [*Friedlingstein et al.*, 1995]. Processes primarily responsible for the land-atmosphere carbon exchange, driven by seasonal and interannual variations in climate, include NPP and organic matter respiration.

[84] NPP follows a light use efficiency formulation [*Field et al.*, 1995]; it is a function of absorbed photosynthetically active radiation (APAR), itself a function of vegetation cover and phenology (LAI) and incoming solar radiation (SRAD). This function is then modulated by high- and low-temperature stress (T) and moisture stress deduced from the actual to potential evapotranspiration (AET/PET).

[85] The heterotrophic respiration formulation, similarly to the one used in LPJ, follows first-order kinetics. The main difference with LPJ lies in the formulations used for the temperature and water control on the decomposition rate. The temperature dependence follows a Q_{10} formulation: $g(T) = Q_{10}^{(T-30)/10}$ where T is the monthly air temperature, and Q_{10} has the value of 2 for all ecosystems. The water dependence follows the CENTURY models [*Parton et al.*, 1993]

$$f(W) = 0.25 \quad \text{if} \quad W < 0.25, \quad \text{(B5)}$$

$$f(W) = W \quad \text{if} \quad 0.25 < W < 1, \quad \text{(B6)}$$

$$f(W) = 2 - W \quad \text{if} \quad 1 < W < 1.75, \quad \text{(B7)}$$

$$f(W) = 0.25 \quad \text{if} \quad W > 1.75, \quad \text{(B8)}$$

where W is the soil water content.

B2. Ocean Carbon Models: OPA and MIT

B2.1. OPA Model

[86] OPA is an ocean general circulation model (OGCM). In this study, it is coupled to an ocean biogeochemistry model. The OGCM has 30 vertical levels, a spatial resolution of 2° in longitude, and a latitudinal resolution that varies from 0.5° in the tropics to 1.5° at high latitudes. It computes vertical mixing explicitly over the entire water column based on a 1.5-order turbulent closure scheme [*Gaspar et al.*, 1990]. Temperature and salinity are restored toward the climatological observations in the interior of the ocean, below the mixed layer, away from ocean-land boundaries, with a restoring timescale of 1 year in the Southern Ocean, and 1 month elsewhere. This restoring dampens long-term variations in ocean physics, but does not affect year-to-year variations associated with changes in mixing depth. The model was forced by a combination of daily to weekly wind stresses and fluxes from satellite and reanalyzed data from 1979 to 1999 as described by *Le Quéré et al.* [2000].

[87] This model reproduces most of the variations in ocean dynamics associated with El-Niño events in the equatorial Pacific but underestimates variability in ocean dynamics at high latitudes. The biogeochemistry part of the model includes plankton dynamics and air-sea CO$_2$ flux [*Aumont et al.*, 2003]. It reproduces partly the local variability in observed surface pCO_2 in the northern subtropics of the Atlantic [*Bates*, 2002] and Pacific [*Karl and Lukas*, 1996] oceans [*Le Quéré et al.*, 2000].

B2.2. MIT Model

[88] Air-sea CO$_2$ fluxes are modeled with an offline biogeochemical model based on the physical fields of the MIT ocean general circulation model [*Marshall et al.*, 1997b, 1997a] that was configured at the Jet Propulsion Laboratory [*Lee et al.*, 2002b]. The ocean general circulation model has 47 vertical levels and a spatial resolution of 1° in longitude and latitudinal resolution varies from 0.3° in the tropics to 1° at high latitudes. For the period 1980–1998, the model is forced with 12-hour variability of reanalyzed wind stress, heat flux, and freshwater flux fields. Comparisons to climatology and time series indicate that the model captures observed mean mixed layer depths and their variability quite well. Comparisons to TOPEX/Poseidon satellite altimetry indicate that the model reproduces all the major features of upper ocean sea surface height variability, but on the global average, only captures 35% of the magnitude of this variability. This finding is consistent with the findings of *Stammer et al.* [1996], who considered the Parallel Ocean Climate Model at 1/4° resolution. Ten-day average output of the physical model forces the biogeochemical model.

[89] The biogeochemical model uses a particle export parameterization with spatial variability to broadly represent the heterogeneity of global export. Temporal variability of surface DIC concentrations compares well to time series observations in the subtropical North Atlantic [*Bates et al.*, 2002] and North Pacific [*Karl and Lukas*, 1996]. The determination of air-sea CO$_2$ exchange and other details are described by *McKinley et al.* [2003, 2004]. Air-sea CO$_2$ flux results shown here for 1980–1998 are detrended to remove the effects of background drift in the model.

Appendix C: Uncertainties in the Inverse Estimates

[90] The inversion returns an error variance-covariance matrix P that is referred to as the "internal error" as in work by *Peylin et al.* [2002]. Note that it also corresponds to the

"within model uncertainty" in work by *Gurney et al.* [2002]. However, *P* refers to the fluxes and not their IAV which are the flux minus the long-term mean. To derive an internal error that strictly applies on the flux IAV only (*P'*), we have to performed the usual computation, $P' = MPM^T$, where *M* is a matrix that describes the linear combinations to obtain flux anomalies from the initial flux estimates. Such computation describes for a linear transformation the statistical projection of a variance-covariance matrix. The resulting uncertainties on the flux IAV (*P'*) will be lower than the uncertainties on the initial fluxes (*P*). Finally, we computed the so-called "external error" from the spread of the seven sensitivity tests that we performed. These errors will partly account for systematic errors such as biases in transport model ("between model error" in work by Gurney et al.).

[91] The change in time of the internal errors directly reflects the size and the distribution of the network. The amplitude of the error reduction is not only associated with the number of new sites assimilated, but it critically depends on their position (given the current network). For instance, over the tropics, the addition of 12 new sites between 1985 and 1990 or of five new South China Sea sites in 1992 produces a similar reduction of internal error for tropical land (Figure 4a). Notice also the increase of the internal error in 1998 for tropical and Northern Hemisphere terrestrial IAV as a few stations were stopped or not available. Given the current level of internal error, it is important to increase or at least maintain the size of the present network. As for external errors (smaller than the internal errors; see Table 3), we should note that we only use two different transport models, recycling 1990 or 1993 winds and one spatial distribution of the fluxes within each region to explore the possible systematic errors. All these results point to the need for increasing the size, the accuracy, and the frequency of the present network.

[92] The internal and external errors are not independent [*Peylin et al.*, 2002] and one should discuss the robustness of the flux IAVs in light of these two uncertainties. The greater the IAV signal is compared to these two errors, the more robust the inverted year-to-year flux variations are. The fact that the IAV signal is similar to or smaller than internal error suggests that statistically we still need more data to assess the year-to-year flux variations at the conventional confidence level of 65%. Secondly, the favorable ratio with the external error suggests that if we trust the main components of our sets of inversions (transport models, spatial patterns, winds, etc.), the IAV signal is then relatively robust, a result that differs from the results of *Peylin et al.* [2002] for the mean carbon fluxes.

[93] To investigate the potential source of uncertainty from using only 1 year of wind, we ran forward the TM3 transport model with the optimized fluxes (from the inversion using TM3) over the 1979–1998 period, using either recycling 1990 winds or the proper winds for each year (ECMWF analyses). We then computed at each site the concentration differences resulting from the interannuality of the transport and further inverted these differences with our inverse set up. Although not strictly equivalent to an inversion with interannual response functions (using the proper winds each year), the residual fluxes obtained can be added to the standard inverse fluxes as corrections due to interannual variations in transport. These corrections do not modify the general picture discussed at the latitudinal or continental scales.

[94] Finally, as for the internal error correlations, negative/positive correlations imply that the inversion cannot fully separate the two regions involved but can only solve for the sum/difference between the two. For example, the highest anticorrelations occur between Northern Hemisphere total land and total ocean (−0.6, Figure 4b). Intuitively, as more stations appear with time and fill some gaps in the network (Figure 1), correlations between regions should decrease. Although this is true for most regions (i.e., anticorrelation between boreal Europe and North Atlantic north goes from −0.4 in 1985 to −0.2 in 1998), few cases show the opposite. Boreal North America becomes more anticorrelated with both the northern part of North Atlantic (from −0.2 in 85 to −0.45 in 95) and temperate North America (not shown) as some stations are added in the early 1990s (BME, BMW, MHT, ICE, ITN). Adding sites always reduces the internal error, but could increase anticorrelations between two regions if their contributions at these sites are similar and rather significant. In our case, the maximum of the response functions from boreal North America at Mace Head is not negligible and comparable for a few months to the North Atlantic response.

References

Archer, D., T. Takahashi, S. Sutherland, J. Goddard, D. Chipman, K. Rodgers, and H. Ogura (1996), Daily, seasonal and interannual variability of sea-surface carbon and nutrient concentration in the equatorial Pacific Ocean, *Deep Sea Res., Part II*, 30, 779–808.

Aumont, O., E. Maier-Reimer, S. Blain, and P. Monfray (2003), An ecosystem model of the global ocean including Fe, Si, P colimitations, *Global Biogeochemical Cycles*, 17(2), 1060, doi:10.1029/2001GB001745.

Bacastow, R. B. (1976), Modulation of atmospheric carbon dioxide by the southern oscillation, *Nature*, 261, 116–118.

Baldocchi, D., E. Falge, and K. Wilson (2001), A spectral analysis of biosphere-atmosphere trace gas flux densities and meteorological variables across hour to multi-year time scales, *Agric. For. Meteorol.*, 107, 1–27.

Bates, N. R. (2002), Interannual variability in the global uptake of CO$_2$, *Geophys. Res. Lett.*, 29(5), 1059, doi:10.1029/2001GL013571.

Bates, N., A. C. Pequignet, R. J. Johnson, and N. Gruber (2002), A variable sink for atmospheric CO$_2$ in subtropical mode water of the North Atlantic Ocean, *Nature*, 420, 489–493.

Battle, M., M. L. Bender, P. P. Tans, J. W. C. White, J. T. Ellis, T. Conway, and R. J. Francey (2000), Global carbon sinks and their variability inferred from atmospheric O$_2$ and δ^{13}C, *Science*, 287, 2467–2469.

Botta, A., N. Ramankutty, and J. Foley (2002), Long-term variations of climate and carbon fluxes over the Amazon basin, *Geophys. Res. Lett.*, 29(9), 1319, doi:10.1029/2001GL013607.

Bousquet, P., P. Peylin, P. Ciais, P. Friedlingstein, C. Lequere, and P. Tans (2000), Interannual CO$_2$ sources and sinks as deduced by inversion of atmospheric CO$_2$ data, *Science*, 290, 1342–1346.

Braswell, B. H., D. S. Schimel, E. Linder, and B. Moore (1997), The response of global terrestrial ecosystems to interannual temperature variability, *Science*, 278, 870–872.

Brix, H., N. Gruber, and C. D. Keeling (2004), Interannual variability of the upper ocean carbon cycle at station ALOHA near Hawaii, *Global Biogeochem. Cycles*, 18, GB4019, doi:10.1029/2004GB002245.

Chedin, A., A. Hollingsworth, N. A. Scott, R. Saunders, M. Matricardi, C. Clerbaux, J. Etcheto, and R. Armante (2003), The feasiblility of

monitoring CO$_2$ from high-resolution infrared sounders, *J. Geophys. Res.*, *108*(D2), 4064, doi:10.1029/2001JD001443.

Ciais, P., et al. (1995), Partitioning of ocean and land uptake of CO$_2$ as inferred by δ^{13}C measurements from the NOAA climate monitoring and diagnostics laboratory global air sampling network, *J. Geophys. Res.*, *100*, 5051–5070.

Ciais, P., et al. (1997), A three-dimensional synthesis study of δ^{18}O in atmospheric CO$_2$: 2. Simulations with the TM2 transport model, *J. Geophys. Res.*, *102*, 5873–5883.

Collatz, G. J., J. T. Ball, C. Grivet, and J. A. Berry (1991), Physiological and environmental regulation of stomatal conductance, photosynthesis and transpiration: A model that includes a laminar boundary layer, *Agric. For. Meteorol.*, *54*, 107–136.

Cox, P. M., R. A. Betts, C. D. Jones, S. A. Spall, and I. J. Totterdell (2000), Acceleration of global warming due to carbon-cycle feedbacks in a coupled climate model, *Nature*, *408*, 184–187.

Cramer, W., D. W. Kicklighter, A. Bondeau, B. Moore, G. Churkina, B. Nemry, A. Ruimy, A. L. Schloss, and the Participants of the Potsdam NPP Model Intercomparison (1999), Comparing global models of terrestrial net primary productivity (NPP): Overview and key results, *Global Change Biol.*, *5*(Suppl. 1), 1–15.

Cramer, W., et al. (2001), Global response of terrestrial ecosystem structure and function to CO$_2$ and climate change: Results from six dynamic global vegetation models, *Global Change Biol.*, *7*, 357–373.

Denning, A. S., G. J. Collatz, C. Zhang, D. A. Randall, J. A. Berry, P. J. Sellers, G. D. Colello, and D. A. Dazlich (1996), Simulations of terrestrial carbon metabolism and atmospheric CO$_2$ in a general circulation model: 1. Surface carbon fluxes, *Tellus, Ser. B*, *48*, 521–542.

Duncan, B. N., R. V. Martin, A. C. Staudt, R. Yevich, and J. A. Logan (2003), Interannual and seasonal variability of biomass burning emissions constrained by satellite observations, *J. Geophys. Res.*, *108*(D2), 4100, doi:10.1029/2002JD002378.

Enting, I. G. (2002), *Inverse Problems in Atmospheric Constituent Transport*, 392 pp., Cambridge Univ. Press, New York.

Farquhar, G. D., and M. L. Roderick (2003), Pinatubo, diffuse light, and the carbon cycle, *Science*, *299*, 1997–1998.

Farquhar, G., S. Von Caemmener, and J. Berry (1980), A biochemical model of photosynthesis CO$_2$ fixation in leaves of C$_3$ species, *Planta*, *149*, 78–90.

Feely, R. A., R. Waninkhof, T. Takahashi, and P. Tans (1999), Influence of El Nino on the equatorial Pacific contribution to atmospheric CO$_2$ accumulation, *Nature*, *398*, 597–601.

Field, C. B., J. T. Randerson, and C. M. Malmström (1995), Global net primary production: Combining ecology and remote sensing, *Remote Sens. Environ.*, *51*, 74–88.

Foley, J. A. (1995), An equilibrium model of the terrestrial carbon budget, *Tellus, Ser. B*, *47*, 310–319.

Francey, R. J., P. P. Tans, C. E. Allison, I. G. Enting, J. W. C. White, and M. Trolier (1995), Changes in oceanic and terrestrial carbon uptake since 1982, *Nature*, *373*, 326–330.

Friedlingstein, P., I. Y. Fung, E. A. Holland, J. G. John, G. P. Brasseur, D. J. Erickson, and D. S. Schimel (1995), On the contribution of the biospheric CO$_2$ fertilization to the missing sink, *Global Biogeochem. Cycles*, *9*, 541–556.

Gaspar, P., Y. Gregoris, and J. M. Lefevre (1990), A simple eddy kinetic energy model for simulations of the oceanic vertical mixing: Tests at station Papa and Long-Term Upper Ocean Study Site site, *J. Geophys. Res.*, *95*, 16,179–16,193.

Gaudry, A. (1993), Report of the 7th WMO meeting of experts on carbon dioxide concentration and isotopic measurement techniques, technical report, World Meteorol. Org., Geneva.

Gerard, J., B. Nemry, L. Francois, and P. Warnant (1999), The interannual change of atmospheric CO$_2$: Contribution of subtropical ecosystems, *Geophys. Res. Lett.*, *26*, 243–246.

Goulden, M. L., J. W. Munger, S. M. Fan, B. C. Daube, and S. C. Wofsy (1996), Exchange of carbon dioxide by a deciduous forest: Response to interannual climate variability, *Science*, *271*, 1576–1578.

Goyet, C., C. Coatanoan, G. Eischeid, T. Amaoka, K. Okuda, R. Healy, and S. Tsunogai (1999), Spatial variation of total CO$_2$ and total alkalinity in the northern Indian Ocean: A novel approach for the quantification of anthropogenic CO$_2$ in seawater, *J. Mar. Res.*, *57*(1), 135–163.

Gruber, N., N. Bates, and C. Keeling (2002), Interannual variability in the North Atlantic Ocean carbon sink, *Science*, *298*, 2374–2378.

Gu, L., D. Baldocchi, S. C. Wofsy, J. W. Munger, J. Michalsky, S. P. Urbanski, and T. A. Boden (2003), Response of a deciduous forest to the Mount Pinatubo eruption: Enhanced photosynthesis, *Science*, *299*, 2035–2038.

Gurney, K. R., et al. (2002), Towards robust regional estimates of CO$_2$ sources and sinks using atmospheric transport models, *Nature*, *415*, 626–630.

Heimann, M. (1995), The global atmospheric tracer model TM2: Model description and user manual, *Tech. Rep. 10*, Max-Planck-Inst. fur Meteorol., Hamburg, Germany.

Jones, C. D., M. Collins, P. M. Cox, and S. A. Spall (2001), The carbon cycle response to ENSO: A coupled climate-carbon cycle model study, *J. Clim.*, *14*, 4113–4129.

Joos, F., R. Meyer, M. Bruno, and M. Leuenberger (1999), The variability in the carbon sinks as reconstructed for the last 1000 years, *Geophys. Res. Lett.*, *26*, 1437–1440.

Kaminski, T., P. J. Rayner, M. Heimann, and I. G. Enting (2001), On aggregation errors in atmospheric transport inversions, *J. Geophys. Res.*, *106*, 4703–4715.

Karl, D. M., and R. Lukas (1996), The Hawaii Ocean Time-series (HOT) program: Background, rationale and field implementation, *Deep Sea Res., Part II*, *43*, 129–156.

Keeling, C. D., and S. C. Piper (2001), Interannual variations of exchanges of atmospheric CO$_2$ and 13CO$_2$ with the terrestrial biosphere and oceans from 1978 to 2000, in *Critical Overview SIO*, pp. 00–24, Scripps Inst. of Oceanogr., La Jolla, Calif.

Keeling, C. D., R. B. Bacastow, A. F. Carter, S. C. Piper, T. P. Whorf, M. Heimann, W. G. Mook, and H. A. Roeloffzen (1989), A three-dimensional model of atmospheric CO$_2$ transport based on observed winds: 1. Analysis of observational data, in *Aspects of Climate Variability in the Pacific and the Western Americas*, *Geophys. Monogr. Ser.*, vol. 55, edited by D. H. Peterson, pp. 165–236, AGU, Washington, D. C.

Keeling, C. D., T. Whorf, M. Wahlen, and J. van der Plicht (1995), Interannual extremes in the rate of rise of atmospheric carbon dioxide since 1980, *Nature*, *375*, 666–670.

Keeling, R. F., S. C. Piper, and M. Heimann (1996), Global and hemispheric CO$_2$ sinks deduced from changes in atmospheric O$_2$ concentration, *Nature*, *381*, 218–221.

Kindermann, J., G. Würth, G. H. Kohlmaier, and F.-W. Badeck (1996), Interannual variation of carbon exchange fluxes in terrestrial ecosystems, *Global Biogeochem. Cycles*, *10*, 737–755.

Knorr, W. (2000), Annual and interannual CO$_2$ exchanges of the terrestrial biosphere: Process-based simulations and uncertainties, *Global Ecol. Biogeogr.*, *9*, 225–252.

Langenfelds, R. L., R. J. Francey, B. C. Pak, L. P. Steele, J. Lloyd, C. M. Trudinger, and C. E. Allison (2002), Interannual growth rate variations of atmospheric CO$_2$ and its δ^{13}C, H$_2$, CH$_4$, and CO between 1992 and 1999 linked to biomass burning, *Global Biogeochem. Cycles*, *16*(3), 1048, doi:10.1029/2001GB001466.

Law, R. M., P. J. Rayner, L. P. Steele, and I. G. Enting (2003), Data and modelling requirements for CO$_2$ inversions using high-frequency data, *Tellus, Ser. B*, *55*(2), 512–521.

Lee, K., D. Karl, R. Wanninkhof, and J. Zhang (2002a), Global estimates of net carbon production in the nitrate-depleted tropical and subtropical oceans, *Geophys. Res. Lett.*, *29*(19), 1907, doi:10.1029/2001GL014198.

Lee, T., I. Fukimori, D. Menemenlis, Z. Xing, and L. Fu (2002b), Effects of Indonesian throughflow on the Pacific and Indian Ocean, *J. Phys. Oceanogr.*, *32*, 1404–1429.

Le Quéré, C., J. C. Orr, P. Monfray, O. Aumont, and G. Madec (2000), Interannual variability of the oceanic sink of CO$_2$ from 1979 through 1997, *Global Biogeochem. Cycles*, *14*, 1247–1265.

Le Quéré, C., O. Aumont, P. Monfray, and J. C. Orr (2003a), Propagation of climatic events on ocean stratification, marine biology, and CO$_2$: Case studies over the 1979–1999 period, *J. Geophys. Res.*, *108*(C12), 3375, doi:10.1029/2001JC000920.

Le Quéré, C., et al. (2003b), Two decades of ocean CO$_2$ sink and variability, *Tellus, Ser. B*, *55*, 649–656.

Lloyd, J., and J. A. Taylor (1994), On the temperature dependence of soil respiration, *Funct. Ecol.*, *8*, 315–323.

Lucht, W., I. C. Prentice, R. B. Myneni, S. Sitch, P. Friedlingstein, W. Cramer, P. Bousquet, W. Buermann, and B. Smith (2002), Climatic control of the high-latitude vegetation greening trend and Pinatubo effect, *Science*, *296*, 1687–1689.

Marshall, J., A. Adcroft, C. Hill, L. Perelman, and C. Heisey (1997a), A finite-volume, incompressible Navier Stokes model for studies of the ocean on parallel computers, *J. Geophys. Res.*, *102*, 5753–5766.

Marshall, J., C. Hill, L. Perelman, and A. Adcroft (1997b), Hydrostatic, quasi-hydrostatic, and nonhydrostatic ocean modeling, *J. Geophys. Res.*, *102*, 5733–5752.

McGuire, A. D. C., et al. (2001), Carbon balance of the terrestrial biosphere in the twentieth century: Analysis of CO₂ climate and land use effects with four process-based ecosystem models, *Global Biogeochem. Cycles*, *15*, 183–206.

McKinley, G. A., M. J. Follows, J. Marshall, and S. Fan (2003), Interannual variability in air-sea O₂ fluxes and the determination of CO₂ sinks using atmospheric O₂/N₂, *Geophys. Res. Lett.*, *30*(4), 1101, doi:10.1029/2002GL016044.

McKinley, G. A., M. J. Follows, and J. Marshall (2004), Mechanisms of air-sea CO₂ flux variability in the equatorial Pacific and the North Atlantic, *Global Biogeochem. Cycles*, *18*, GB2011, doi:10.1029/2003GB002179.

Meentemeyer, V. (1978), Macroclimate and lignin control of litter decomposition rates, *Ecology*, *59*, 465–472.

Myneni, R., C. Keeling, C. Tucker, G. Asrar, and R. Nemani (1997), Increased plant growth in the northern latitudes from 1981 to 1991, *Nature*, *386*, 698–702.

National Oceanic and Atmospheric Administration (2000), GLOBALVIEW - CO₂: Cooperative Atmospheric Data Integration Project–Carbon dioxide [CD-ROM], technical report, Boulder, Colo. (Available via anonymous FTP at ftp.cmdl.noaa.gov, path: ccg/CO₂/GLOBALVIEW)

Nemani, R., M. White, P. Thornton, K. Nishida, S. Reddy, J. Jenkins, and S. Running (2002), Recent trends in hydrologic balance have enhanced the terrestrial carbon sink in the United States, *Geophys. Res. Lett.*, *29*(10), 1468, doi:10.1029/2002GL014867.

Page, S. E., F. Siegert, J. Rieley, H. Boehm, A. Jaya, and S. Limin (2002), The amount of carbon released from peat and forest fires in Indonesia during 1997, *Nature*, *420*, 61–65.

Parton, W. J., et al. (1993), Observations and modeling of biomass and soil organic matter dynamics for the grassland biome worldwide, *Global Biogeochem. Cycles*, *7*, 785–809.

Peylin, P., P. Bousquet, C. Ciais, and P. Monfray (1999), Differences of CO₂ flux estimates based on a time-independent versus a time-dependent inversion method, in *Inverse Methods in Global Biogeochemical Cycles*, *Geophys. Monogr. Ser.*, vol. 114, edited by P. Kasibhatla, M. Heimann, and D. Hartley, pp. 295–309, AGU, Washington, D. C.

Peylin, P., D. Baker, P. Bousquet, J. Sarmiento, P. Ciais, and P. Monfray (2002), Influence of atmospheric transport uncertainty on annual mean versus seasonnal inversions of atmospheric CO₂ data, *J. Geophys. Res.*, *107*(D19), 4385, doi:10.1029/2001JD000857.

Rayner, P., I. Enting, R. Francey, and R. Langenfelds (1999), Reconstructing the recent carbon cycle from atmospheric CO₂, δ¹³C and O₂/N₂ observations, *Tellus, Ser. B*, *51*, 213–232.

Rödenbeck, C., S. Houweling, M. Gloor, and M. Heimann (2003), CO₂ flux history 1982–2001 inferred from atmospheric data using a global inversion of atmospheric transport, *Atmos. Chem. Phys.*, *3*, 1919–1964.

Sarmiento, J. L., T. M. C. Hughes, R. J. Stouffer, and S. Manabe (1998), Simulated response of the ocean carbon cycle to anthropogenic climate warming, *Nature*, *393*, 245–249.

Schimel, D., and D. Baker (2002), Carbon cycle: The wildfire factor, *Nature*, *2*, 29–30.

Scholze, M., J. O. Kaplan, W. Knorr, and M. Heimann (2003), Climate and interannual variability of the atmosphere-biosphere ¹³CO₂ flux, *Geophys. Res. Lett.*, *30*(2), 1097, doi:10.1029/2002GL015631.

Siegert, F., G. Ruecker, A. Hinrichs, and A. A. Hoffmann (2001), Increased damage from fires in logged forest during droughts caused by El Niño, *Nature*, *414*, 437–440.

Sitch, S., et al. (2003), Evaluation of ecosystem dynamics, plant geography and terrestrial carbon cycling in the LPJ Dynamic Global Vegetation Model, *Global Change Biol.*, *9*, 161–185.

Smith, B., I. C. Prentice, and M. T. Sykes (2001), Representation of vegetation dynamics in the modelling of terrestrial ecosystems: Comparing two contrasting approaches within european climate space, *Global Ecol. Biogeogr.*, *10*(6), 621–637.

Stammer, D., R. Tokmakian, A. Semtner, and C. Wunsch (1996), How well does a 1/4° global circulation model simulate large-scale oceanic observations?, *J. Geophys. Res.*, *101*, 25,779–25,811.

Takahashi, T., R. A. Feely, R. Weiss, R. H. Wanninkhof, D. W. Chipman, S. C. Sutherland, and T. T. Takahashi (1997), Global air-sea flux of CO₂: An estimate based on measurements of sea-air P_CO₂ difference, in *Proceedings of the National Academy of Science*, vol. 94, p. 8929, Natl. Acad. of Sci., Washington, D. C.

Takahashi, T., et al. (2002), Global sea-air CO₂ flux based on climatological surface ocean pCO₂, and seasonal biological and temperature effects, *Deep Sea Res., Part II*, *49*, 1601–1622.

Thonicke, K., S. Venevsky, S. Sitch, and W. Cramer (2001), The role of fire disturbance for global vegetation dynamics: Coupling fire into a Dynamic Global Vegetation Model, *Global Ecol. Biogeogr.*, *10*, 661–677.

Tian, H., J. M. Melillo, D. W. Kicklighter, A. D. McGuire, J. V. K. Helfrich III, B. Moore III, and C. J. Vorosmarty (1998), Effect of interannual climate variability on carbon storage in Amazonian ecosystems, *Nature*, *396, 664–667.*

Trudinger, C. M., I. G. Enting, R. J. Francey, D. M. Etheridge, and P. J. Rayner (1999), Long-term variability in the global carbon cycle inferred from a high precision CO₂ and δ¹³C ice core record, *Tellus, Ser. B*, *51*, 233–248.

van der Werf, G. R., J. T. Randerson, J. Collatz, and L. Giglio (2003), Carbon emissions from fires in tropical and subtropical ecosystems, *Global Change Biol.*, *9*, 547–562.

Wanninkhof, R. (1992), Relationship between wind speed and gas exchange over the ocean, *J. Geophys. Res.*, *97*, 7373–7382.

White, W., and R. Peterson (1996), An antarctic circumpolar wave in surface pressure, wind, temperature and sea-ice extent, *Nature*, *4*, 699–702.

Winguth, A. M. E., M. Heimann, K. D. Kurz, E. Maier-Reimer, U. Mikolajewics, and J. Segschneider (1994), El Niño-Southern Oscillation related fluctuations of the marine carbon cycle, *Global Biogeochem. Cycles*, *8*, 39–63.

Winn, C., Y. Li, F. Mackenzie, and D. Karl (1998), Rising surface ocean dissolved inorganic carbon at the Hawaii ocean time-series site, *Mar. Chem.*, *15*, 33–47.

Zimov, S. A., S. P. Davidov, G. M. Zimova, A. I. Daviodova, F. S. Champin, M. C. Chapin, and J. F. Reynolds (1999), Contribution of disturbance to increasing seasonal amplitude of atmospheric CO₂, *Science*, *284*, 1973–1976.

————————————

P. Bousquet, Université de Versailles Saint Quentin en Yvelines, F-78035 Versailles, France.

P. Ciais and P. Friedlingstein, Laboratoire des Sciences du Climat et de l'Environnement, Commissariat à l'Energie Atomique, L'orme des Merisiers, F-91191 Gif sur Yvette, France.

N. Gruber, IGPP and Department of Atmospheric Sciences, University of California, Los Angeles, Los Angeles, CA, USA.

C. Le Quéré, Max-Planck-Institut für Biogeochemie, Postfach 100164, D-07701 Jena, Germany.

G. McKinley, Department of Atmospheric and Oceanic Sciences, University of Wisconsin-Madison, Madison, WI, USA.

P. Peylin, Laboratoire Biogéochimie des Milieux Continentaux INRA-CNRS-UPMC, INRA-INAPG, F-78850 Thiverval-Grignon, France. (peylin@lsce.saclay.cea.fr)

P. Rayner, CSIRO Atmospheric Research, PMB 1 Aspendale, Victoria 3195, Australia.

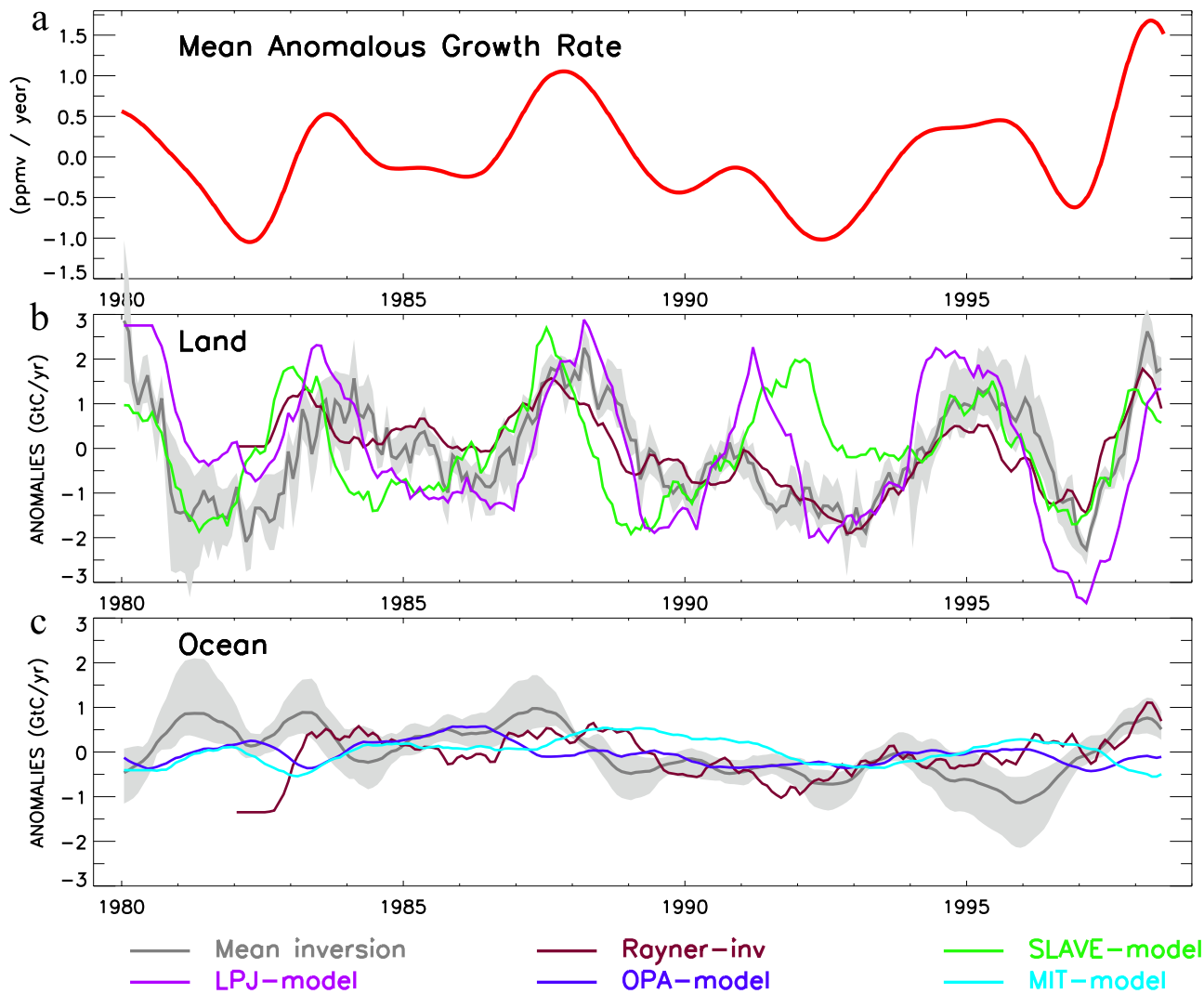S. Sitch, MetOffice (JCHMR), Maclean Building, Crowmarsh Gifford, Wallingford, Oxfordshire OX10 8BB, UK.

Figure 2. (a) Mean anomalous gross rate obtained from the data at all stations of Figure 1. (b, c) Global land and global ocean flux anomalies over 1980–1998 (in GtC per year) as obtained from our ensemble of inversions (gray zone defines the range of all inversions, and dark line denotes the mean), from *Rayner et al.* [1999], from the SLAVE land surface model [*Friedlingstein et al.*, 1995], from the LPJ land surface model [*Sitch et al.*, 2003], from the OPA-HAMOCC3 ocean model [*Le Quéré et al.*, 2000], and from the MIT ocean model [*McKinley et al.*, 2003].
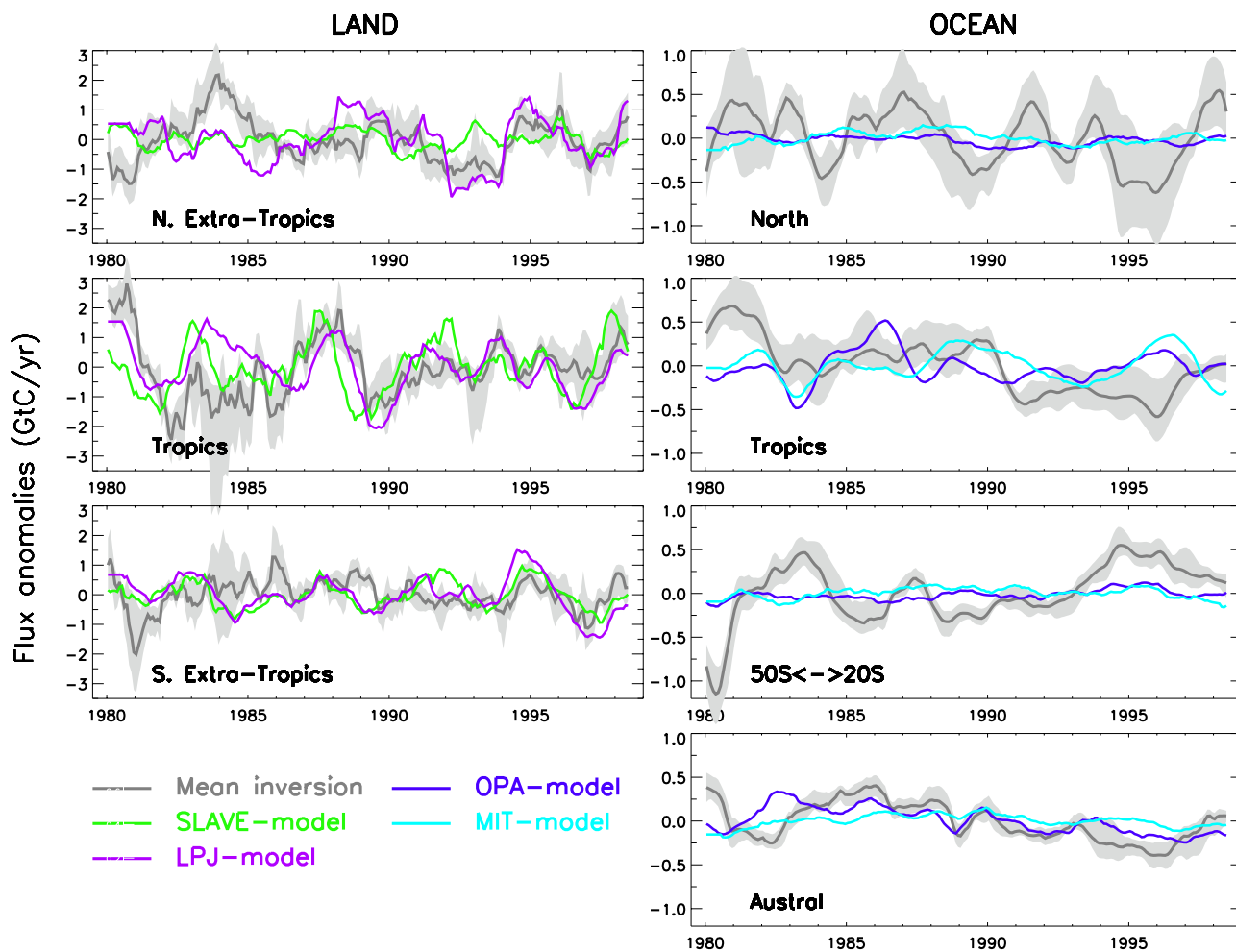
Figure 3. Regional land and ocean flux anomalies over 1980–1998 (in GtC per year) for the Northern extratropical land and ocean (>20°N), the tropical land and ocean, the southern extratropical land (<20°S), the temperate Southern Ocean (50°S–20°S), and the austral ocean. Gray zone and color lines correspond to the different estimates as in Figure 2.
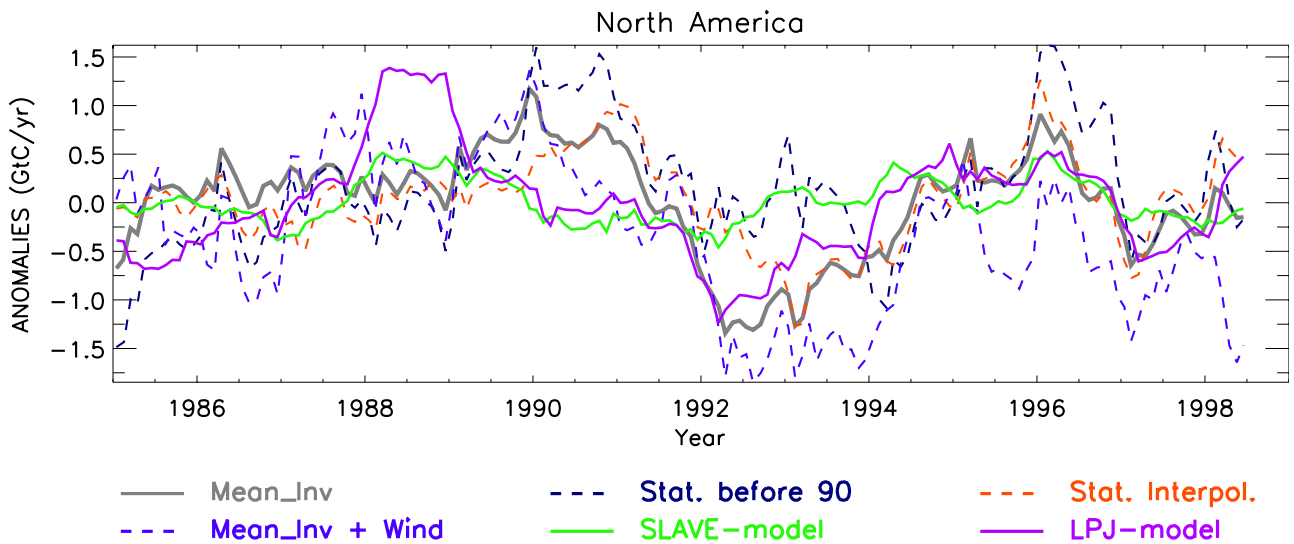
Figure 7. Flux IAV estimated for North America (three individual regions of Figure 1 grouped together) for different inverse setup and for bottom-up models: mean inversion (black), inversion where we stop assimilating new stations after 1989 (dark blue), inversion with all 67 sites extrapolated over the entire period (1980–1998) from Globalview (orange), and mean inversion plus some corrections computed from the interannual wind experiment (i.e., inversion of the concentration differences from a direct simulation with and without interannual winds; see section 3.3; light blue).
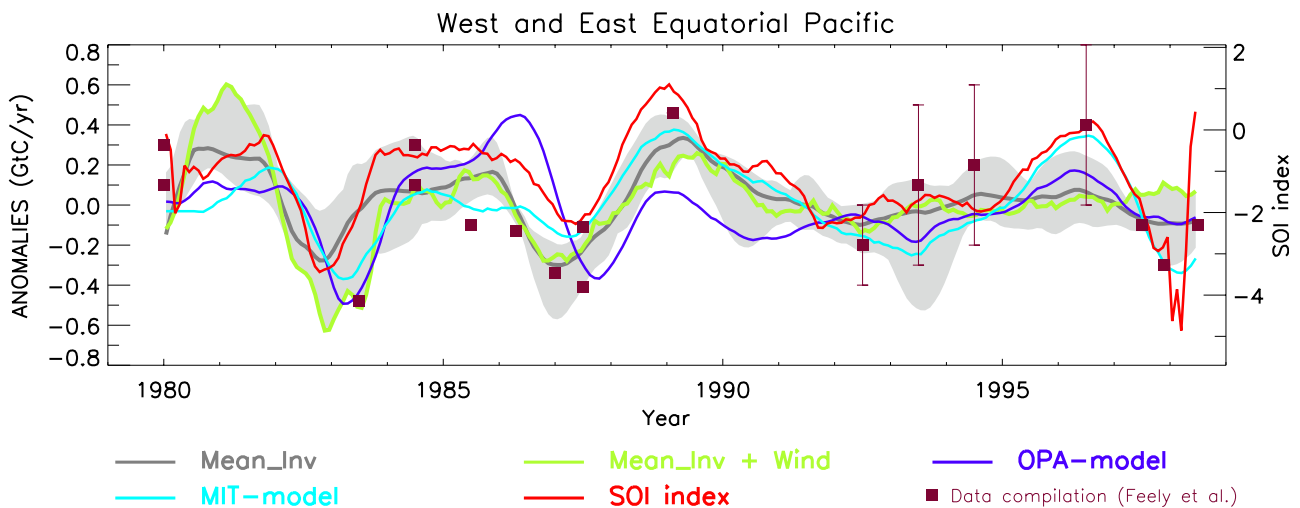

Figure 8. Flux anomalies for the equatorial Pacific Ocean from our ensemble of inversions (gray zone for the full range and dark line for the mean), from the mean inversion plus some corrections computed from the interannual wind experiment (i.e., inversion of the concentration differences from a direct simulation with and without interannual winds; see section 3.3), from the OPA and MIT ocean models, and from a compilation of oceanic data [*Feely et al.*, 1999]. The SOI index is overplotted (right axis).